Structural and biophysical analysis of a *Haemophilus influenzae* tripartite ATP-independent periplasmic (TRAP) transporter

Michael J. Currie[1]†, James S. Davies[1,2]†, Mariafrancesca Scalise[3], Ashutosh Gulati[2], Joshua D. Wright[1], Michael C. Newton-Vesty[1], Gayan S. Abeysekera[1], Ramaswamy Subramanian[4], Weixiao Y. Wahlgren[5], Rosmarie Friemann[6], Jane R. Allison[7], Peter D. Mace[8], Michael D.W. Griffin[9], Borries Demeler[10,11], Soichi Wakatsuki[12,13], David Drew[2], Cesare Indiveri[3], Renwick C.J. Dobson[1,9]* & Rachel A. North[2]*

[1] Biomolecular Interaction Centre, Maurice Wilkins Centre for Biodiscovery, MacDiarmid Institute for Advanced Materials and Nanotechnology, and School of Biological Sciences, University of Canterbury, PO Box 4800, Christchurch 8140, New Zealand.

[2] Department of Biochemistry and Biophysics, Stockholm University, 106 91 Stockholm, Sweden.

[3] Department DiBEST (Biologia, Ecologia, Scienze della Terra) Unit of Biochemistry and Molecular Biotechnology, University of Calabria, Via P. Bucci 4C, 87036 Arcavacata di Rende, Italy.

[4] Biological Sciences and Biomedical Engineering, Bindley Bioscience Center, Purdue University, 1203 W State St, West Lafayette, IN 47906, USA.

[5] Department of Chemistry and Molecular Biology, Biochemistry and Structural Biology, University of Gothenburg, Box 462, 40530 Gothenburg, Sweden.

[6] Centre for Antibiotic Resistance Research (CARe) at University of Gothenburg, Box 440, 40530 Gothenburg, Sweden.

[7] Biomolecular Interaction Centre, Digital Life Institute, Maurice Wilkins Centre for Molecular Biodiscovery, and School of Biological Sciences, University of Auckland, Auckland 1010, New Zealand.

[8] Biochemistry Department, School of Biomedical Sciences, University of Otago, Dunedin 9054, New Zealand.

[9] Bio21 Molecular Science and Biotechnology Institute, Department of Biochemistry and Pharmacology, University of Melbourne, Parkville, Victoria 3010, Australia.

[10] Department of Chemistry and Biochemistry, University of Montana, Missoula, MT, USA.

[11] Department of Chemistry and Biochemistry, University of Lethbridge, Lethbridge, AB, Canada.

[12] Biological Sciences Division, SLAC National Accelerator Laboratory, Menlo Park, CA 94025, USA.

[13] Department of Structural Biology, Stanford University School of Medicine, Stanford, CA 94305, USA.

†These authors contributed equally to this work

*For correspondence

rachel.north@dbb.su.se or renwick.dobson@canterbury.ac.nz

Keywords: sialic acid, Neu5Ac, protein-protein interaction, membrane transport proteins, transport mechanism

Abstract

Tripartite ATP-independent periplasmic (TRAP) transporters are secondary-active transporters that receive their substrates via a soluble binding protein to move bioorganic acids across bacterial or archaeal cell membranes. Recent cryo-EM structures of TRAP transporters provide a broad framework to understand how they work, but the mechanistic details of transport are not yet defined. Here we report the cryo-EM structure of the *Haemophilus influenzae N*-acetylneuraminate TRAP transporter (*Hi*SiaQM) at 2.99 Å resolution (extending to 2.2 Å at the core), revealing new features. The improved resolution (the previous *Hi*SiaQM structure is 4.7 Å resolution) permits accurate assignment of two Na^+ sites and the architecture of the substrate binding site, consistent with mutagenic and functional data. Moreover, rather than a monomer, the *Hi*SiaQM structure is a homodimer. We observe lipids at the dimer interface, as well as a lipid trapped within the fusion that links the SiaQ and SiaM subunits. We show that the affinity (K_D) for the complex between the soluble *Hi*SiaP protein and *Hi*SiaQM is in the micromolar range and that a related SiaP can bind *Hi*SiaQM, highlighting features of the complex interface. This work provides key data that enhances our understanding of the 'elevator-with-an-operator' mechanism of TRAP transporters.

(*197 words*)

Introduction

Secondary-active transporters are found in all domains of life (1-3). They catalyse the movement of molecules across membranes, exploiting the free energy associated with electrochemical ion gradients to drive transport [see (4,5) for recent reviews on the topic]. In bacteria, secondary-active transporters are used for both the export of toxic compounds and for the import of nutrients needed for cell growth (4,6).

The import of carbohydrates across the plasma membrane is a key process for bacteria, particularly those pathogenic bacteria that adopt a scavenging lifestyle within their host (7). For *Haemophilus influenzae*, a Gram-negative opportunistic pathogen, the ability to uptake host-derived sialic acids is important for pathogenesis (8). Sialic acids are a diverse family of nine-carbon carbohydrates, and in humans, sialic acids are highly abundant in the respiratory and gastrointestinal tracts where they coat glycoconjugates as terminal sugars (7,9). The most common sialic acid found in humans is *N*-acetylneuraminate (Neu5Ac) (7). To gain a growth advantage in these environments, bacteria such as *H. influenzae* evolved the ability to utilise host-derived sialic acid as a nutrient source (**Figure 1**). The sialic acid catabolic pathway provides an alternative source of carbon, nitrogen and energy, and has been identified in 452 bacterial species, most of which are mammalian pathogens or commensals (10). Alongside degradation, and perhaps more importantly, *H. influenzae* uses sialic acids to coat its lipopolysaccharide surface, and this sialylation in turn provides camouflage and protection from the human immune response (11,12). *H. influenzae* lacks the *de novo* sialic acid biosynthetic pathway, so sialic acids must be scavenged and transported into the cell (13). Engineered *H. influenzae* strains that are unable to transport sialic acids into the cell have decreased virulence in animal models—evidence that the sialic acid transport pathway is a viable therapeutic target (14) and others have already developed inhibitors to sialic acid transporters (15). The sole sialic acid transporter in *H. influenzae* belongs to the tripartite ATP-independent periplasmic (TRAP) transporter family.

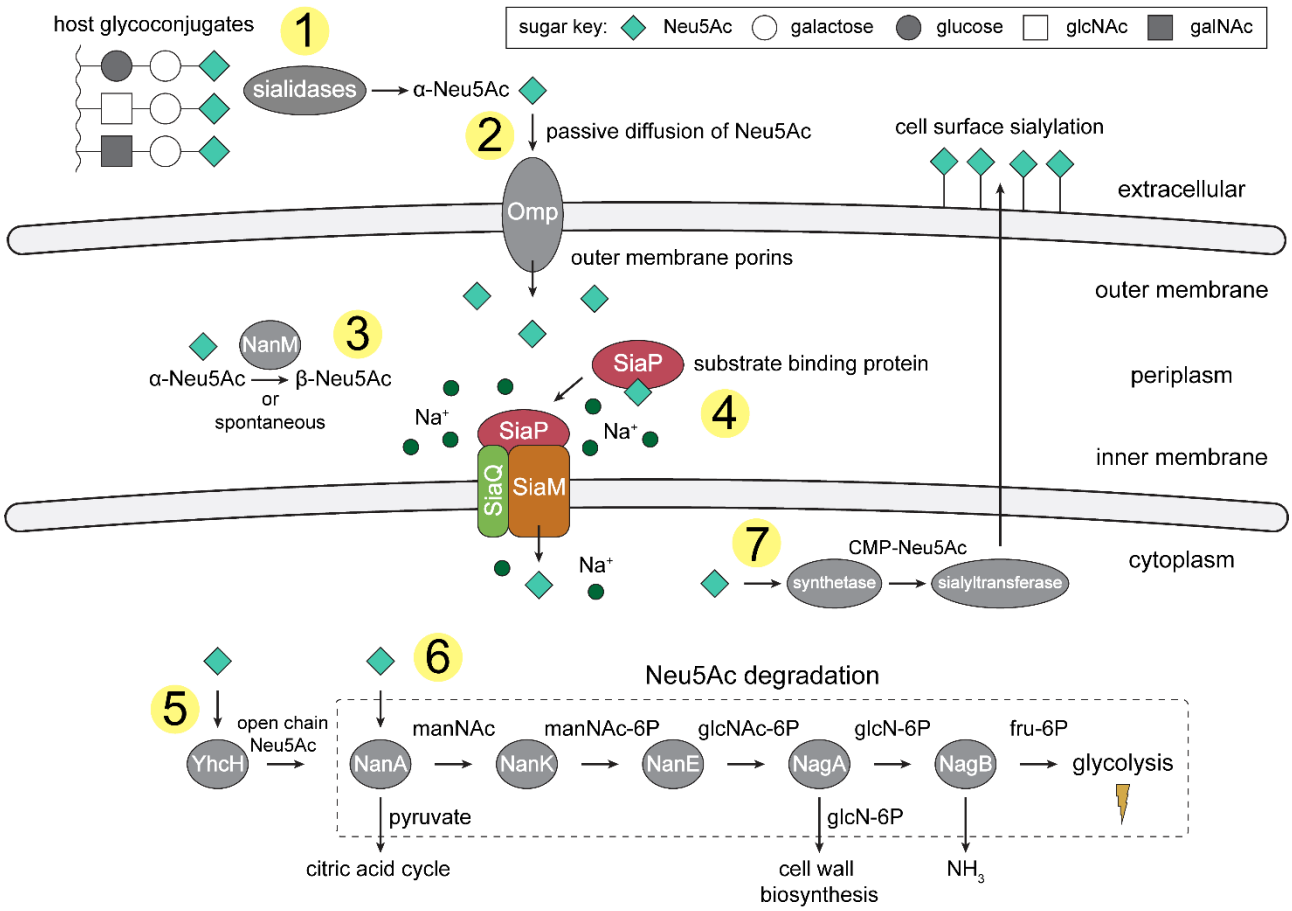

Figure 1 | An overview of Neu5Ac metabolism in *H. influenzae*. 1) *H. influenzae* is sialidase negative and relies on environmental sialidases to hydrolyse and release terminal Neu5Ac from human glycoconjugates. 2) Outer membrane porins facilitate diffusion of Neu5Ac into the periplasm. 3) A mutarotase, NanM, catalyses the formation of β-Neu5Ac from α-Neu5Ac to prepare for active transport across the inner membrane. 4) Neu5Ac is captured by the high-affinity substrate-binding protein, SiaP. SiaP delivers Neu5Ac to the SiaQM TRAP transporter, which uses a Na^+ electrochemical gradient to drive transport. *H. influenzae* cannot synthesise Neu5Ac and relies solely on SiaPQM for obtaining environmental Neu5Ac. 5) Cytoplasmic processing of Neu5Ac by an anomerase, YhcH, generates the unfavourable open chain form in preparation for use by the first enzyme of the Neu5Ac degradation pathway, NanA. 6) Neu5Ac is sequentially degraded into cell wall constituents or fructose-6-phosphate, which can enter glycolysis. Five conserved enzymes (an aldolase, NanA; kinase, NanK; epimerase, NanE; deacetylase, NagA; and deaminase, NagB) are involved in this pathway which provides *H. influenzae* with carbon, nitrogen, and energy. 7) Alternatively, Neu5Ac can be activated by cytidine monophosphate and a sialic acid synthetase and added to lipooligosaccharides by a sialyltransferase. Definitions: Neu5Ac, *N*-acetylneuraminate; manNAc, *N*-acetylmannosamine; manNAc-6P, *N*-acetylmannosamine-6-phosphate; glcNAc, *N*-acetylglucosamine; glcNAc-6P, *N*-acetylglucosamine-6-phosphate; glcN-6P, glucosamine-6-phosphate; fru-6P, fructose-6-phosphate; galNAc, *N*-acetylgalactosamine; CMP, cytidine monophosphate; Omp, outer membrane porin; NanM, Neu5Ac mutarotase; YhcH, Neu5Ac anomerase; NanA, Neu5Ac lyase; NanK, manNAc kinase; NanE, manNAc-6P epimerase; NagA, glcNAc-6P deacetylase; NagB, glcN-6P deaminase.

Tripartite ATP-independent periplasmic (TRAP) transporters are a major class of secondary-active transporters found only in bacteria and archaea (16,17). They use energetically favourable cation gradients to drive the import of specific carboxylate-containing nutrients against their concentration-

gradient, including C_4-dicarboxylates, α-keto acids, aromatic substrates, amino acids and sialic acids (18). A functional TRAP system is made up of a soluble substrate-binding 'P-subunit', and a membrane-bound complex comprising a small 'Q-subunit' and a large 'M-subunit'. For most TRAP transporters the Q- and M-subunits are separate polypeptides (19,20), but in ~25% of sequences [InterPro analysis (21)] the Q- and M-subunit polypeptides are fused into a single polypeptide (16). TRAP transporters are different from almost all other secondary-active transporters in that they can only accept substrates from the P-subunit (22). Analogous to ABC importers, the P-subunit is secreted into the periplasm to capture host-derived substrates with high affinity and specificity. The substrate-loaded P-subunit subsequently delivers the substrate to the membrane transporter (Q- and M-subunits) (18,23-25).

The SiaPQM system from *H. influenzae* has fused Q- and M-subunits and is one of the best characterised TRAP systems to date (11,23,24,26,27), with key functional and biophysical studies informing a putative transport mechanism driven by a Na^+ gradient (28). Before transport into the cell by SiaPQM, sialidases release sialic acids from the terminal position of host glycoconjugates (**Figure 1**). *H. influenzae* is, however, sialidase negative and relies on the sialidases of other bacteria to generate free sialic acids (29). In Gram-negative bacteria, sialic acids diffuse into the periplasm through an outer membrane porin, such as the general porins OmpF or OmpC in many bacteria, Omp P2 in *H. influenzae* (30,31), or by using a Neu5Ac specific porin such as NanC (32). The substrate-binding protein SiaP (P-subunit) binds Neu5Ac in the periplasm with high-affinity, undergoing a ligand-induced conformational change to a closed state (23-26). It is this closed form that then delivers Neu5Ac to the membrane bound Q- and M-subunits. This protein-protein interaction and the subsequent transport of Neu5Ac through the transmembrane subunits are not yet characterised. In particular, the conformational changes that take place for both SiaP and SiaQM to allow alternating access of the transporter have not been fully elucidated, though we have suggested previously that the binding of the closed P-subunit must induce either a global elevator-type motion or a local gating rearrangement as a part of an elevator mechanism (33). These changes allow the transporter to bind Neu5Ac and Na^+ at the periplasmic side and transport them into the cytoplasm.

Here, we report the high-resolution cryo-EM structure of *Hi*SiaQM in amphipol and demonstrate that in detergent, amphipol and a nanodisc environment the fused *H. influenzae* SiaQM membrane subunits can stably exist as both monomeric (QM) and homodimeric (2QM) states. We determined the homodimeric (2QM) structure of *Hi*SiaQM using single particle cryo-electron microscopy, the first structure of a fused TRAP transporter at near atomic resolution (2.99 Å, with local resolution extending to ~2.2 Å), which reveals new details of the transport mechanism. The structure, combined with functional and biophysical data, supports the hypothesis that *Hi*SiaQM operates using the

'elevator-with-an-operator' mechanism that we proposed for TRAP transporters (33).

Results

The cryo-EM structure of Hi*SiaQM reveals a dimeric configuration.*

We assessed the stability of *Hi*SiaQM in several detergents that solubilise *Hi*SiaQM from *Escherichia coli* membranes. Lauryl maltose neopentyl glycol (L-MNG) led to more stable protein preparations compared to dodecyl-β-D-maltoside (DDM) (**Supplementary Figure 1a**), which has been used previously (20,27). Curiously, *Hi*SiaQM purified with a high L-MNG concentration elutes as a major peak at 65 mL with a significant shoulder at 58 mL and this elution profile is reversed at a low L-MNG concentration (**Supplementary Figure 1a**)—a signature of a self-association, suggesting *Hi*SiaQM forms higher order oligomers. By comparison, the non-fused monomeric *Photobacterium profundum* SiaQM (*Pp*SiaQM) does not show this behaviour when expressed with the same purification tag and purified in the same low concentration of L-MNG, eluting at 67 mL, which we have previously shown to correspond to a monomeric species (33) (**Supplementary Figure 1a**).

We decided to purify *Hi*SiaQM using L-MNG under conditions that favour the larger species for the following reasons: 1) we were previously unsuccessful at determining the cryo-EM structure of the monomer, because of the small size of the protein (72 kDa) and lack of features outside of the micelle or nanodisc that makes particle alignment difficult; 2) even with a megabody bound to increase the size and provide asymmetric features, other structural investigation on monomeric *Hi*SiaQM led to only moderate resolution data, which may reflect some instability or heterogeneity in the sample; and 3) we reasoned that avoiding fiducial markers such as nanobodies and megabodies would also allow exploration of the conformational dynamics of the transporter without any binder-associated bias. Thus, the larger *Hi*SiaQM species was isolated by exchanging purified protein out of L-MNG detergent and into amphipol A8-35, an amphipathic polymer used to solubilise and stabilise membrane proteins.

*Hi*SiaQM comprises two distinct dimeric configurations in approximately equal quantities (36%) in the 14,281-image dataset (**Figure 2a, Supplementary Figure 2, Supplementary Table 1**). Dimeric *Hi*SiaQM exists either as a side-by-side parallel dimer where both monomers face the same way, or an antiparallel dimer where one monomer is rotated around the dimer interface 180° relative to the other (**Figure 2a, Supplementary Figure 2**). Dimerisation is mediated by the same interface in both of these structures but given that *Hi*SiaP is found in the periplasm and SiaQM requires SiaP to function, the parallel dimer is most likely the physiologically relevant conformation. The maps are of high resolution (overall 2.9 Å for the antiparallel dimer and 3.2 Å for the parallel dimer, FSC = 0.143

criterion) with both extending to 2.2 Å at the core, allowing for accurate fitting of helices and (almost) all side chains (**Supplementary Figure 3**). The dimeric particles allowed for structure determination without a protein fiducial marker bound (*e.g.*, nanobody or antigen-binding fragment), which was required to solve the structure of the monomeric *Pp*SiaQM (33) and the low resolution monomeric *Hi*SiaQM (27).

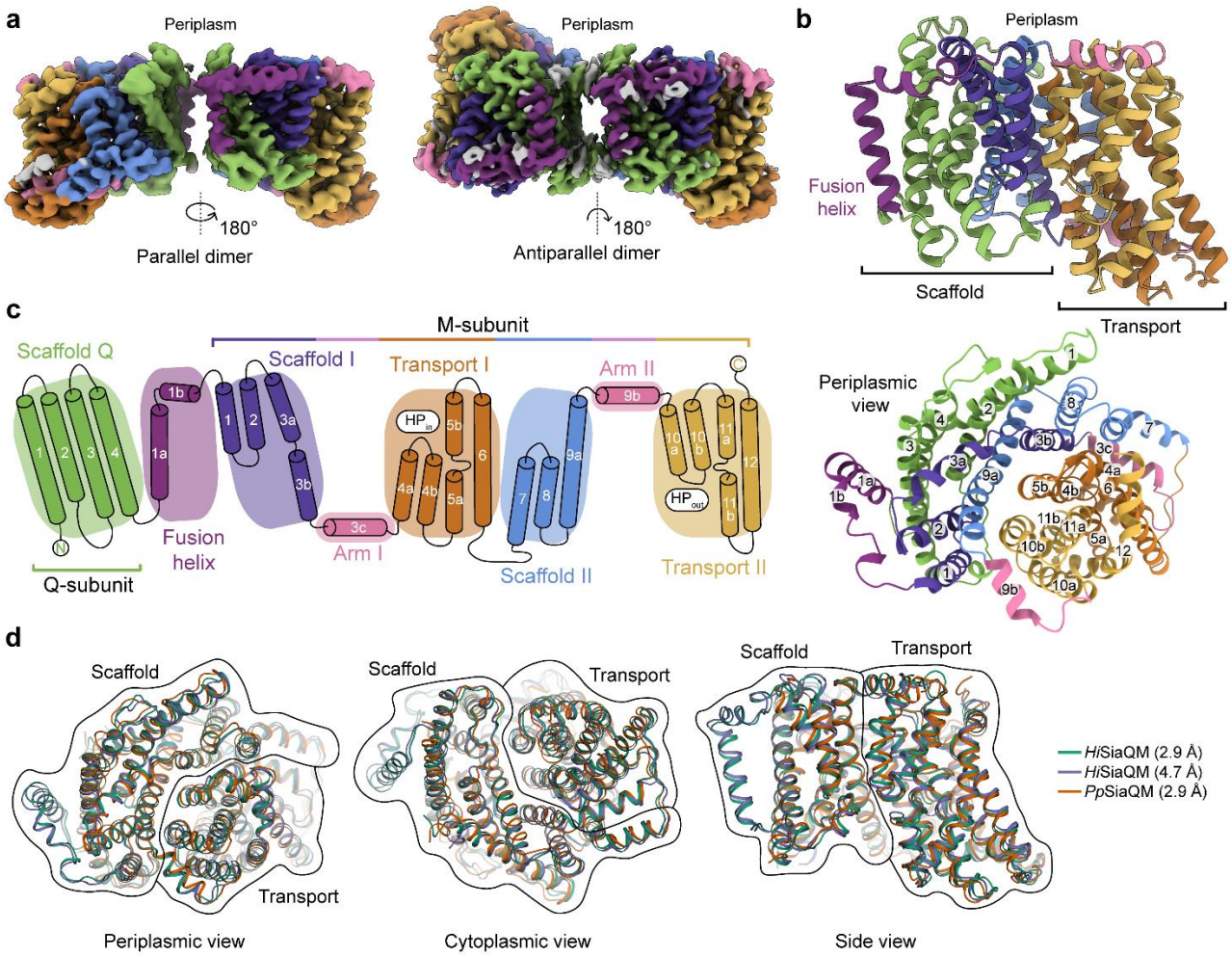

Figure 2 | The structure of *Hi*SiaQM. **a**, Coulomb maps for the parallel (3.36 Å) and antiparallel (2.99 Å) *Hi*SiaQM homodimers. The periplasmic surfaces of the monomers are facing the same direction for the parallel dimer (PDB: 8THI), whereas the periplasmic surface of one monomer is rotated 180° for the antiparallel dimer (PDB: 8THJ). The transport domain (orange and gold) is in the 'elevator down' conformation in all four monomers. The dimeric interface in both maps is distanced and neither has significant protein-protein interactions. The maps are coloured according to the topology in **c**. Density consistent with phospholipids is coloured grey and is particularly present in the dimer interface of the higher resolution antiparallel dimer map. **b**, Structural model of the *Hi*SiaQM monomer. The transport domain is in the 'elevator down' conformation with the substrate binding site facing the cytoplasm. **c**, The topology of *Hi*SiaQM is the same as the non-fused *Pp*SiaQM with the addition of the fusion helix. The M-subunit forms the transport domain (orange and gold) and bracing arm helices (pink) as well as a large portion of the scaffold (purple and blue). The Q-subunit is entirely used as a scaffold for the elevator transport mechanism. The fusion helix (purple) connects the scaffold and adds to its size. It also forms a short horizontal helix, similar to the arm helices of the M-subunit. **d**, A structural overlay of *Hi*SiaQM (2.9 Å structure, green; 4.7 Å

structure, purple) and *Pp*SiaQM (2.9 Å structure, orange) shows that the helices of the structures are well aligned, and all three structures are in the same conformation.

In all four *Hi*SiaQM protomers the transport domain is in the inward-open conformation ('elevator down'), which is the substrate release state (r.m.s.d. for alignment = ~0.2 Å, **Figure 2a,b**). This is the same conformation as the previous megabody-bound *Pp*SiaQM structures in amphipol and a nanodisc (33) and also the same as the recently reported low resolution (4.7 Å) megabody-bound *Hi*SiaQM structure in a nanodisc (27). Three-dimensional variability analysis (3DVA) (34) of our *Hi*SiaQM reconstructions shows only very subtle motion at the dimer interface, and does not show any global elevator motions in the final reconstruction (**Supplementary Movie 1**). That we observe the inward-open conformation without either a bound P-subunit or fiducial marker, suggests that this is the resting state of the transporter.

Both dimers form through an interface between the Q-subunits of the monomers. The relatively flat sides of the Q-subunits are positioned adjacent to each other in an interface that is not intimately connected by side chain interactions (**Figure 2a**). When refined using dimeric masks, the parallel dimer has slightly lower resolution at the dimer interface (scaffold region), compared to the antiparallel dimer. Local refinement of each monomer within the parallel dimer improved the resolution at the scaffold region, suggesting this is perhaps a relatively dynamic interface. The buried interface area is small (~200 $Å^2$) for the antiparallel configuration, and even smaller (~100 $Å^2$) for the parallel configuration (35). Further still, the parallel interface area is formed by a small number of residues at the N-termini, which have modest resolution. The majority of the interface for these dimers must therefore be mediated by lipid molecules that bridge between the monomers, some of which we observe directly in the cryo-EM maps (discussed later). Small interfaces have been observed in the elevator-type Na^+/H^+ antiporter NhaA from *E. coli* (36) and throughout the SLC26 family (37) (also elevator-type), but the *Hi*SiaQM interfaces are much smaller than other dimeric ion transporter superfamily members, such as the TRAP related symporter VcINDY, a divalent anion/Na^+ symporter (DASS) from *Vibrio cholerae* (38-40), and the antimicrobial efflux pumps MtrF (41) and YdaH (42), which are all elevator-type homodimers with buried interface areas of ~1800–2100 $Å^2$.

The topology of *Hi*SiaQM is similar to the non-fused *Pp*SiaQM, aside from the additional fusion helix that links the Q- and M-subunits across the membrane (**Figure 2c**). The helix starts on the cytoplasmic side, packing against the Q-subunit and crossing the membrane vertically, then turns 90° and runs laterally (perpendicular to the membrane) before forming a loop and connecting to the M-subunit on the periplasmic side (**Figure 2a-c**). An overlay with the recently determined SiaQM structures shows that the main chains are similar (*Pp*SiaQM to high resolution *Hi*SiaQM r.m.s.d. = 1.2 Å across 520 C_α-atoms and low resolution *Hi*SiaQM to high resolution *Hi*SiaQM r.m.s.d. = 1.0

Å across 571 C_α-atoms, **Figure 2d**). All three structures are in the 'elevator down' conformation with close alignment between the 16-17 helices (**Figure 2d**). Differences in the loops of the proteins exist, including the positioning of the 'clamshell' loops of the Na^+ binding sites (discussed later).

Hi*SiaQM exists in a stable monomer-dimer self-association.*

The oligomeric assembly of TRAP transporters within the membrane has implications for the transport cycle, as well as the interaction between SiaP and SiaQM. Secondary-active transporters can exist as monomers (43,44), or as larger multimeric complexes of oligomers (45,46). For example, VcINDY (38-40), MtrF (41) and YdaH (42) all share the same fold and have a dimeric structure (47). These elevator-type transporters form oligomers at the scaffold domains, which is thought to provide the stability needed for elevator movements of the transport domain. Recently, a TRAP related fused transporter belonging to the TAXI (TRAP-Associated eXtracytoplasmic Immunogenic proteins) TRAP subfamily from *Proteus mirabilis* also eluted as two peaks during size exclusion chromatography, signalling a likely self-association (48). In contrast, the non-fused TRAP transporter *Pp*SiaQM uniquely functions as a monomer (1QM) (33), where instead of homodimerisation, the scaffold is formed by heterodimerisation of the Q- and M-subunits. Recent work on *Hi*SiaQM also proposes a monomeric (1QM) functional transporter (20,27). However, our high resolution dimeric cryo-electron microscopy structures and the self-association behaviour observed from size exclusion chromatography (**Supplementary Figure 1a**) infer a stable dimeric architecture for *Hi*SiaQM is probable.

To further support this result, *Hi*SiaQM purified in L-MNG and DDM was characterised by sedimentation velocity analytical ultracentrifugation (SV-AUC), resulting in two distinct species in each of the samples (**Figure 3a, Supplementary Figure 4-6**). As there were no contaminants following purification (**Supplementary Figure 1b**), the two species represent a protein self-association, consistent with that observed during purification. The oligomeric state of the two species was verified using SV-AUC analysis that compares the measured masses with theoretical masses. This suggests that *Hi*SiaQM is present as a monomer and a dimer in both L-MNG (**Figure 3a**) and DDM (**Supplementary Figure 4**). The two species have sedimentation coefficients (all are corrected for water and 20 °C unless otherwise specified) of 7.3 S and 9.9 S in L-MNG, and 7.6 S and 10.3 S in DDM. The calculated frictional ratios for the monomeric species are 1.2 in L-MNG and 1.1 in DDM. These are consistent with a globular particle, as we would expect for a protein in a detergent micelle. The calculated frictional ratios for the dimeric species are 1.2 in L-MNG and 1.0 in DDM, which are also consistent with a globular particle.

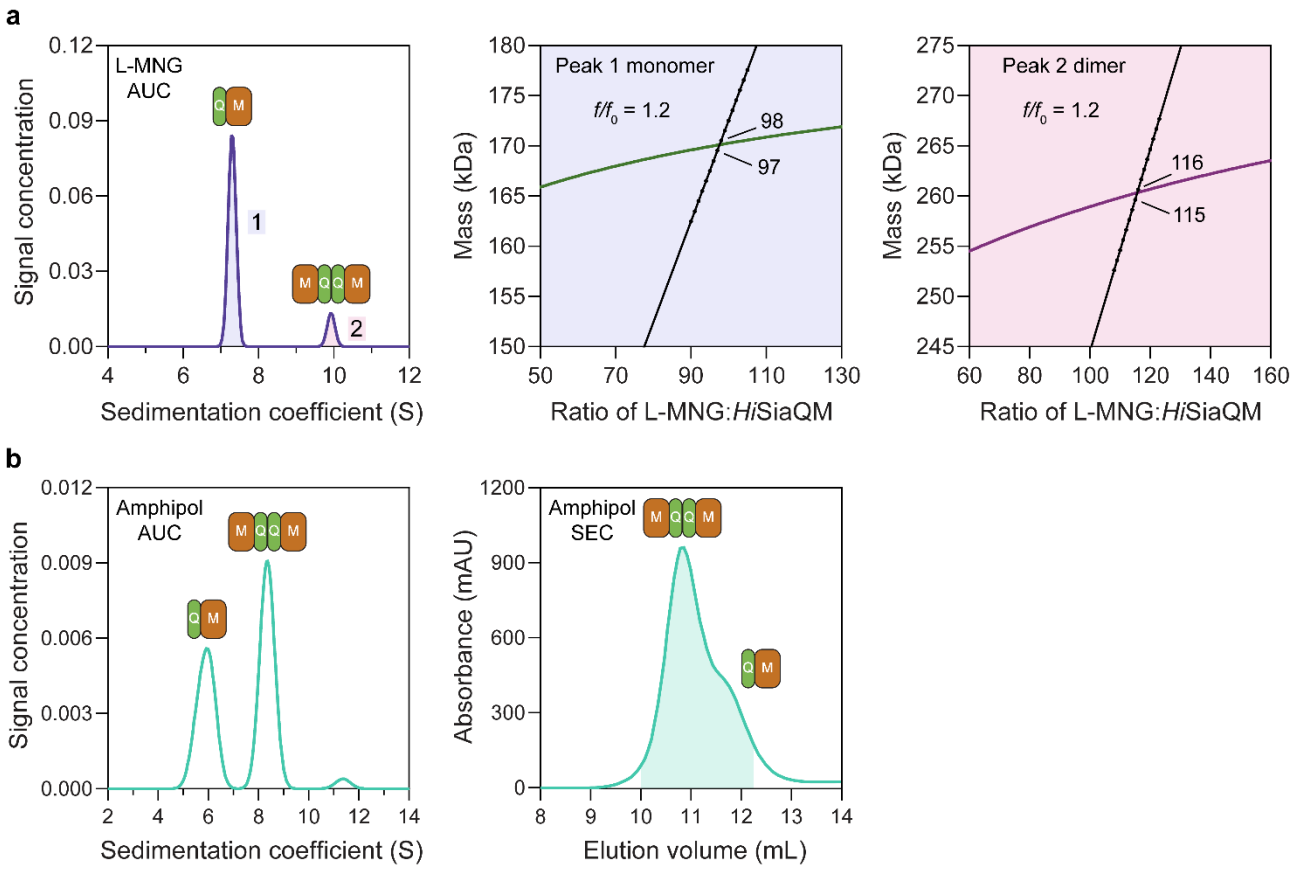

Figure 3 | *Hi*SiaQM self-association in L-MNG and amphipol. a, SV-AUC analysis of *Hi*SiaQM in L-MNG (left panel). Two well resolved species exist at 7.3 S and 9.9 S, with the larger peak constituting 85% of the signal. The species at 7.3 S (Peak 1, blue shading) is most consistent with *Hi*SiaQM as a monomer with ~98 molecules of L-MNG bound (middle panel; green = measured mass, black = theoretical mass); Peak 1 existing as a dimer is unlikely, as the dimeric protein would only have ~14 molecules of L-MNG bound. The calculated f/f_0 of a monomer for Peak 1 is 1.2, consistent with a protein in a detergent micelle. The species at 9.9 S (Peak 2, pink shading) is most consistent with *Hi*SiaQM as a dimer with ~116 molecules of L-MNG bound (right panel; purple = measured mass, black = theoretical mass); Peak 2 existing as a monomer is not possible, as the protein clearly has a smaller species in Peak 1 and cannot be divided further than a monomer, and a trimer is also unlikely as the trimeric protein would only have ~32 molecules of L-MNG bound. The calculated f/f_0 of a dimer for Peak 2 is also 1.2, again consistent with a protein in a detergent micelle. These calculations do not account for bound lipid molecules. **b**, Left panel, SV-AUC analysis of amphipol solubilised *Hi*SiaQM (initially purified in L-MNG) shows two distinct species present at 5.9 S and 8.3 S. These are monomeric and dimeric species, as L-MNG solubilised protein exists as these oligomeric states at 7.3 S and 9.9 S as in **a**. Right panel, representative size exclusion chromatogram of amphipol solubilised *Hi*SiaQM favouring the dimeric state. The main peak at ~10.8 mL contains dimeric *Hi*SiaQM and the shoulder at ~11.8 mL contains monomeric *Hi*SiaQM. The sample used for structure determination is shaded turquoise.

We then solubilised *Hi*SiaQM in amphipol (A8-35) and nanodiscs (cNW11, ~11 nm in diameter (49)) to ascertain whether these systems might afford better stability and again found two species consistent with a monomer and a dimer. SV-AUC analysis of amphipol solubilised protein (**Figure 3b**) is consistent with a monomer at 5.9 S and a dimer at 8.3 S, when considering the oligomeric information obtained from SV-AUC in L-MNG (**Figure 3a**). In nanodiscs, a reconstitution ratio of 1:4:80 of

*Hi*SiaQM:MSP:lipid (MSP = membrane scaffold protein) resulted in multiple peaks during size exclusion chromatography (**Supplementary Figure 7a**). Three fractions across the elution profile were analysed with SV-AUC and the main species in each had sedimentation coefficients of 4.0 S, 6.8 S, and 9.0 S (**Supplementary Figure 7b**). The species at 4.0 S is most consistent with empty nanodiscs and the species at 6.8 S and 9.0 S are most consistent with nanodiscs containing monomeric and dimeric *Hi*SiaQM, respectively (**Supplementary Figure 7b**).

To summarise, we have demonstrated that *Hi*SiaQM can exist in a monomer-dimer state in two detergents, amphipol and nanodiscs, which mimic the native environment. The proposal that *Hi*SiaQM forms dimers within the plasma membrane is supported by the observation that a stable dimer with low aggregation propensity forms when solubilised in L-MNG (**Supplementary Figure 1a,** blue trace). Stable species also exist when solubilised in amphipol (**Figure 3b**), particularly evidenced by the collection of cryo-EM data to <3 Å resolution. Under the same L-MNG detergent conditions, similar concentrations, and with an identical Ni^{2+} affinity tag, non-fused *Pp*SiaQM does not show this behaviour (**Supplementary Figure 1a**)—evidence that dimerisation is a result of a self-association and not the Ni^{2+} affinity tag or cohabitation, where the number of available micelles is low enough that two proteins cohabitate the same micelle for stable solubilisation. The dimeric assembly of *Hi*SiaQM is consistent with other examples of transporters that use the elevator-type mechanism (*e.g.*, VcINDY (38-40)), but clearly different from that reported recently for *Pp*SiaQM and *Hi*SiaQM TRAP transporters (27,33).

Lipid binding sites.

As a transporter, *Hi*SiaQM has evolved alongside lipids, which are increasingly shown to be important for general transporter function and oligomerisation (50-52). Evident in our cryo-EM maps are well-defined phospholipid densities associated with areas of *Hi*SiaQM that appear to be important for the function of an elevator-type mechanism (**Figure 4**). The two most compelling areas are the dimer interface and a lipid binding pocket formed by the fusion helix.

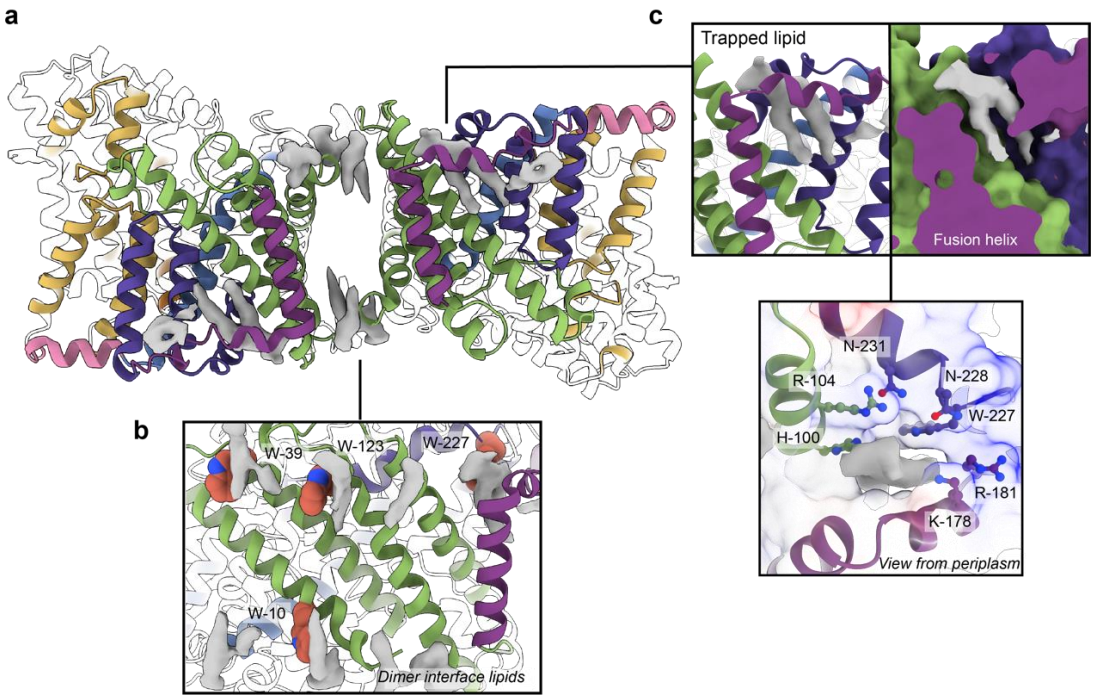

Figure 4 | Phospholipids bound to *Hi*SiaQM. a, The dimer has well-defined areas of density (grey) that correspond to bound phospholipids. Two mechanistically important areas are the dimer interface and fusion helix pocket. **b**, Phospholipids are present at the dimer interface, including in close contact with the anchoring tryptophan residues (shown as spheres) of the Q-subunits that provide stability to the scaffold domain. **c**, A single phospholipid is trapped in a pocket formed by the fusion helix (protein model surface shown in colour, EM density in grey). The lipid is on the periplasmic side of the transporter and the headgroup appears to be coordinated by residues surrounding the top of the pocket, which have a generally positive character.

There is a void region at the dimer interface in both structures that likely contains amphipol polymers and lipids. Indeed, we observe density for lipids in this region (best seen in the slightly higher resolution antiparallel dimer) (**Figure 2a**, **Figure 4b**). Notably, these densities are adjacent to tryptophan residues (**Supplementary Figure 8**), known for their role in anchoring membrane proteins (53), and one of the positions is where we also observe clear lipid density in the *Pp*SiaQM structure in a nanodisc (33). The discovery of these annular lipids is surprising given that the protein was first extracted and extensively purified in L-MNG detergent, followed by exchange into A8-35 amphipol for cryo-EM studies. There are some weaker densities around the periphery of the protein that likely correspond to amphipol, but we can confidently identify densities for phospholipids given their distinctive hairpin shape (**Figure 4**). That lipids have remained bound in this area through the isolation and purification supports that these are specific and strong interactions, which thereby anchor the scaffold domain in the membrane. The lipids at this interface may also have a role in strengthening dimerisation, as seen in other secondary-active transporters such as NhaA (36,51).

The architecture of the fusion helix leaves a pocket between the lateral part of the helix and the main bundle of the transporter. A closer inspection of the map density shows that a distinct hairpin-shaped

phospholipid density is positioned in this pocket (**Figure 4c**). This enclosed pocket appears to tightly fit only one phospholipid, which is presumably trapped here during protein folding. Several residues from the scaffold portion are well-poised to interact with a lipid headgroup, including H100, R104, K178 and W227 (**Figure 4c**). Analysis of the electrostatic surface of the pocket shows a significant amount of positive charge. We suggest that this site likely binds a negatively charged phospholipid and have modelled phosphatidylglycerol into the density. The predicted interacting residues are not well conserved amongst fused TRAP transporters (**Supplementary Figure 8**), which is possibly a reflection of varying bacterial membrane compositions.

This site and the presence of a lipid were not identified in the recent structure of *Hi*SiaQM in a nanodisc (containing only the zwitterionic lipid DMPC)—instead, amino acids are modelled to fill the hydrophobic pocket. This is notable, as Peter et al. (27) hypothesised that W227 is important for the SiaP:SiaQM interaction, and show that mutation of this residue to an arginine significantly affects bacterial growth in an *in vivo* growth assay. The resolution of our structures allows us to unambiguously model this residue facing away from the surface and engaged in an interaction with the trapped phospholipid, further supporting our identification of tryptophan residues in anchoring roles in the scaffold of TRAP transporters (33). This finding is important in the context of the transport mechanism used by *Hi*SiaPQM. As the identified phospholipid is intercalated between scaffolding helices and is very close to the putative SiaP:SiaQM interface, it is feasible that this site is physiologically significant and may influence the stability of the transporter or even the conformational dynamics of the entire system. We emphasise that this phospholipid binding pocket is not present in *Pp*SiaQM, which may point to differences in the dynamics of the scaffolds and how the scaffold interacts with SiaP in non-fused systems.

Neu5Ac and Na^+ binding sites.

Although others have already demonstrated Neu5Ac transport for the *Hi*SiaPQM system (28), we verified that our recombinant *Hi*SiaPQM is active after solubilisation in the previously untested detergent L-MNG. Time-dependent uptake of [^{3}H]-Neu5Ac was measured after reconstituting *Hi*SiaQM into potassium containing proteoliposomes (**Figure 5a**). This method allows for the transport dependence on a Na^+ gradient ($\Delta\mu Na^+$, generated by adding external Na^+) or a membrane potential (Ψ, generated by adding valinomycin) to be measured (54).

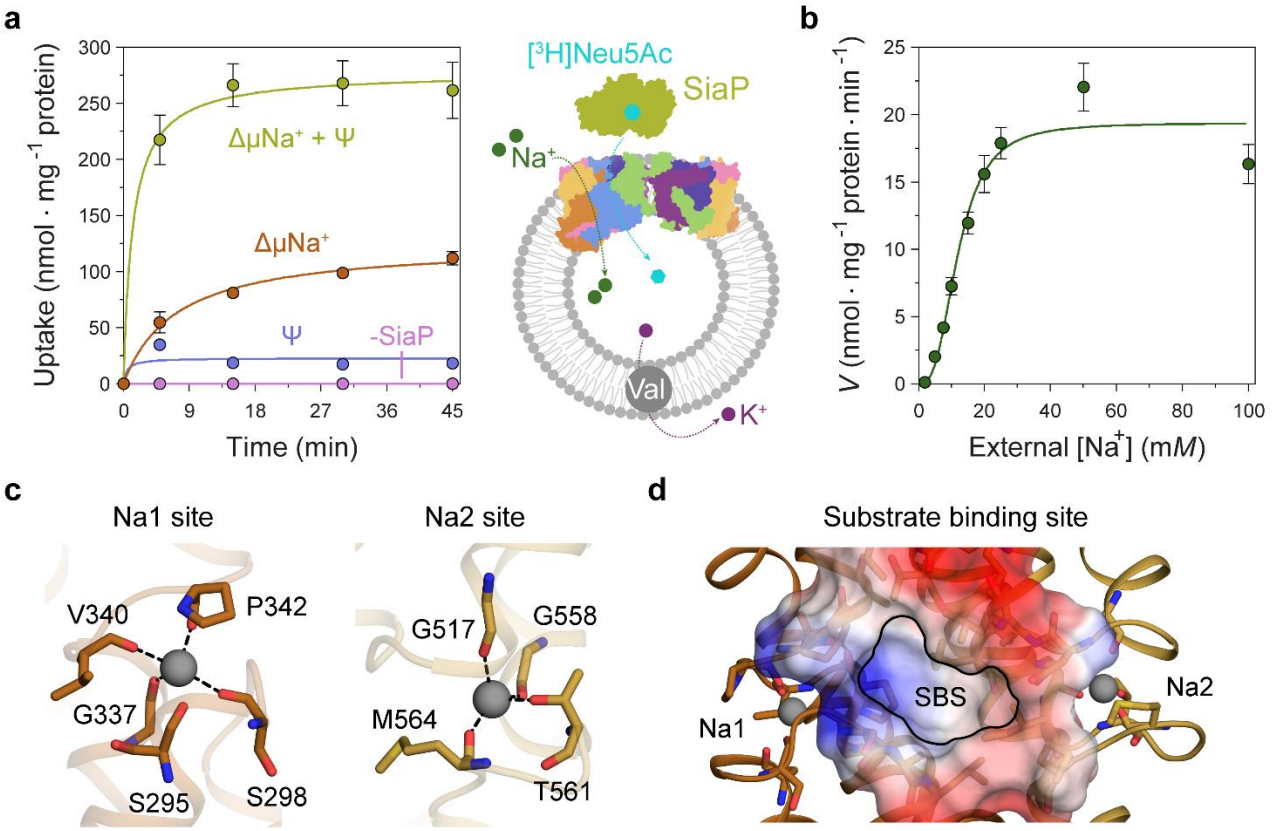

Figure 5 | Transport assays demonstrate that L-MNG solubilised *Hi*SiaQM is functional. **a**, [^{3}H]-Neu5Ac uptake was measured at multiple time intervals under each condition and used to calculate transport rates. *Hi*SiaQM had the highest activity in the presence of *Hi*SiaP, a membrane potential and a Na^+ gradient (green circles). Approximately one-third of this rate was present without a membrane potential (orange circles). Transport was low in the absence of Na^+ (blue circles) and negligible without *Hi*SiaP (pink circles). Error bars represent the standard error of the mean (SEM) for three technical replicates, except without *Hi*SiaP, which has two replicates. The assay diagram contains the parallel *Hi*SiaQM structure, coloured by topology as in **Figure 2a**,**c**. This is for visual presentation; it is not known if the transporter exists as a dimeric species in the assay. **b**, The rate of transport is dependent on the concentration of Na^+, showing a sigmoidal response [Hill coefficient = 2.9 (95% C.I. 2.2–3.9)]. The K_M for Na^+ is 12 mM (95% C.I. 10–14 mM). The displayed response shows that *Hi*SiaPQM operates close to its maximum measured rate at a reasonably low external Na^+ concentration (25 mM). Error bars represent the SEM of five technical replicates. **c**, Two Na^+ binding sites (Na1 and Na2) were identified in *Hi*SiaQM. These sites share highly similar coordinating residues with *Pp*SiaQM. At the Na1 site, a Na^+ ion (grey) is coordinated by the carbonyl groups of S298, G337, V340 and P342 (orange sticks, coordination shown as black dashes). S295 is also shown but its carbonyl is positioned just outside the coordination distance in our structure. At the Na2 site, a Na^+ ion (grey) is coordinated by the carbonyl groups of G517, G558 and M564, and the side chain hydroxyl of T561 (gold sticks, coordination shown as black dashes). **d**, A putative substrate binding site (SBS, outlined) is located in the transport domain of *Hi*SiaQM (orange and gold). The mostly hydrophobic binding site (shown as sticks and electrostatic surface) exists between the two Na^+ binding sites and is large enough to bind Neu5Ac.

Transport by *Hi*SiaQM was dependent on a Na^+ gradient ($\Delta\mu Na^+$) (**Figure 5a**, green and orange circles) and was stimulated 3-fold in the presence of a membrane potential (Ψ) (**Figure 5a**, green circles). *Hi*SiaP is required for transport since without external *Hi*SiaP transport was negligible. These results agree with previous work on *Hi*SiaQM purified in decyl-β-D-maltoside (DM) (28) and

show that our tagged construct is active and not inactivated by L-MNG. Net transport by *Hi*SiaQM is electrogenic, as activity is enhanced when an inside negative membrane potential (Ψ) is imposed (**Figure 5a**). Since Neu5Ac has a single negative charge at neutral pH, electrogenic transport means two or more Na^+ ions are transported for every Neu5Ac imported. Varying external [Na^+] at a fixed substrate concentration resulted in a Hill coefficient of 2.9 (95% confidence interval = 2.2–3.9), implying that at least two Na^+ ions are co-transported during each transport cycle (**Figure 5b**). These data are consistent with the previous work (28), as well as the stoichiometry we recently determined for *Pp*SiaQM (33).

The fused *Hi*SiaPQM system has higher transport activity than the non-fused *Pp*SiaPQM system. With the same experimental setup used for *Pp*SiaPQM (5 μM Neu5Ac, 50 μM SiaP) (33), the accumulation of [^{3}H]-Neu5Ac is ~10-fold greater. This difference may reflect the origins of each transporter system—*P. profundum* is a deep-sea bacterium and as such the transporter is required to be functional at low temperatures and high pressures. In contrast, *H. influenzae* is mesophilic, found in the human respiratory tract and therefore more likely to show native-like rates in ambient experimental conditions. A similar pattern has been reported for the elevator transporter Glt_{Ph}, where transporters from hyperthermophilic species are slow, and mesophilic versions are faster (55). These organisms also vary substantially in membrane lipid composition, which is currently too difficult to test in this experimental setup.

Next, we examined the *Hi*SiaQM Na^+ binding sites in our cryo-EM structure (**Figure 5c**). The higher resolution antiparallel dimer structure shows density for Na^+ ions at both Na1 and Na2 sites (**Supplementary Figure 9a**), confirming the sites we identified and tested in *Pp*SiaQM (33), and also the aforementioned stoichiometry of Na^+ ions transported determined in the *Hi*SiaQM proteoliposome assay (28). The Na1 and Na2 sites across all four monomers are highly similar, although subtly different to those reported previously (**Supplementary Figure 9b**). The resolution of the structures allows for the unambiguous assignment of side chain positions at these binding sites and enables mechanistically important residues to be distinguished.

At the Na1 site, coordination is achieved by the backbone carbonyls of S298, G337, V340 and P342 in a tetrahedral pattern, with a valence = 1, as determined by CheckMyMetal (56,57). The backbone carbonyl of S295 is also positioned for coordination but is slightly further away at 2.9/3.0 Å. In contrast, the equivalent carbonyl in *Pp*SiaQM (S103) is closely associated with the Na^+ ion to form a trigonal bipyramidal coordination pattern. Na2 coordination is achieved by the backbone carbonyls of G517, G558 and M564, and the side chain hydroxyl of T561, which together coordinate the Na^+ ion in a tetrahedral pattern with a valence = 1.2/1.3. In contrast to the Na2 site of *Pp*SiaQM, the

backbone carbonyl of T561 is positioned further away at 4.2 Å distance and does not directly coordinate the Na^+ ion in our structure. In the *Pp*SiaQM structure, the equivalent residue (T369) coordinates the Na^+ ion with both the side chain and main chain of T561 to form a square planar coordination pattern. S298, P342, G517 and G558 are highly conserved in TRAP transporters; S295, G337 and T561 sometimes vary as other small residues and V340 and M564 often vary as other hydrophobic side chains (**Supplementary Figure 8**). S298A did not show an effect on growth when mutated to alanine previously (27) and therefore may not be considered mechanistically important, but our structure shows that it coordinates Na1 through the backbone carbonyl, masking the effect of the side chain mutation.

Our structures have a large cytoplasm-facing solvent-accessible cavity housing the putative binding site for Neu5Ac that is flanked by the Na1 and Na2 Na^+ ion sites (**Figure 5d**), similar to *Pp*SiaQM. The dataset was collected without Neu5Ac and not surprisingly, there is no ligand density in the binding sites. The putative Neu5Ac binding site is lined with residues S300, A301, L302, P338, S343, I344, A345, I348, D521, A522, L523, Q526, T552, M555, M556, I559 and M566 of the transport domain which form a largely hydrophobic binding site (**Figure 5d**). This site is large enough to bind Neu5Ac and is more defined than previously reported (**Supplementary Figure 9c**). Residues D304 and D521 each have a significant effect on bacterial growth when mutated to alanine and were thought to be involved in Na^+ ion or substrate binding (27). Our structure shows that neither are involved in Na^+ binding and although D521 does line the substrate binding pocket and introduces some charge to the site, D304 faces away from the substrate binding site and instead coordinates the residues that bind the Na^+ ion at the Na1 site.

On the formation of the tripartite complex.

The observation that *Hi*SiaQM can form a dimer has implications for the mechanism of transport, and as yet the affinity for the SiaP:SiaQM complex has not been directly established. To address this, we used analytical ultracentrifugation with fluorescence detection to determine the affinity between *Hi*SiaP and *Hi*SiaQM in the presence of Neu5Ac. Fluorescein isothiocyanate (FITC) was used to fluorescently label *Hi*SiaP, with the labelling conditions adjusted to provide just one FITC label per *Hi*SiaP protein. This allowed for a usable signal to be obtained at 10 nM *Hi*SiaP and minimised any inhibitory effects on complex formation, as 22 of the 31 lysine residues of *Hi*SiaP are spatially distant from the putative interacting surface. Titrating *Hi*SiaQM in L-MNG to 40 µM (a 4000-fold excess over *Hi*SiaP, 10 nM) in the presence of 5 mM Neu5Ac resulted in the development of two peaks at ~7.5 S and ~10.5 S (**Figure 6a**). Integration of the signal that shifted to a larger species resulted in ~40% of the *Hi*SiaP bound at the highest concentration of *Hi*SiaQM (40 µM). This experiment

allowed us to estimate a K_D for the complex of 65 µM (95% confidence interval = 62–69 µM, **Figure 6b**). Avoiding non-ideality meant that we could only use concentrations of *Hi*SiaQM approaching the K_D, but the binding model fit was very good (R^2 = 0.99). This is in agreement with previous work that used surface plasmon resonance with biotin immobilised *Hi*SiaQM in DDM, where a K_D of ~1 µM was estimated, but it was stressed that the true K_D is very likely weaker due to the inability to fit a 1:1 binding model (27), which may have been complicated by the presence of dimeric *Hi*SiaQM or aggregation.

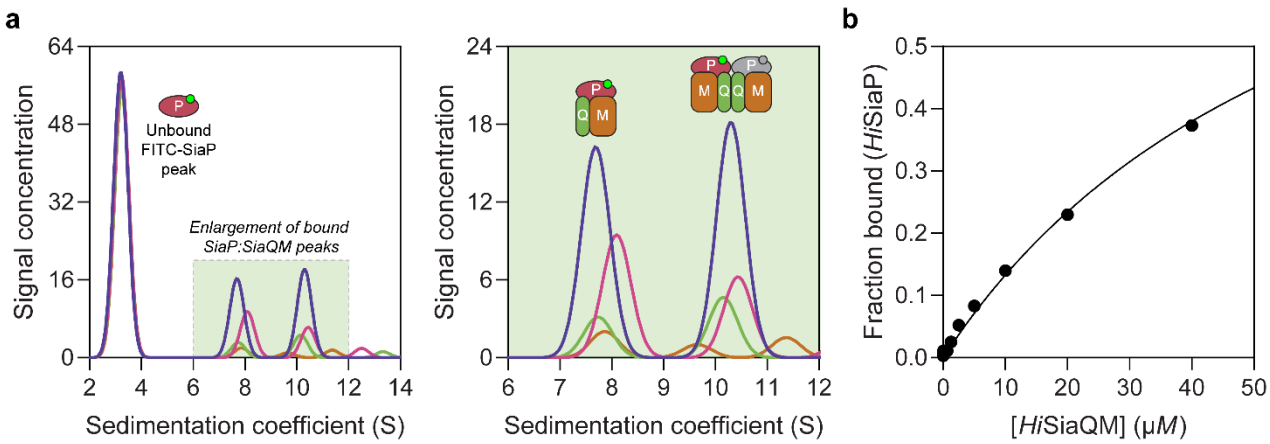

Figure 6 | Sedimentation velocity AUC analysis of the interaction between *Hi*SiaQM and *Hi*SiaP in L-MNG detergent. **a**, Titrating increasing concentrations of *Hi*SiaQM (blue, 40 µM (2.88 mg/mL); pink, 20 µM; green, 10 µM; brown, 5 µM; other concentrations omitted for clarity) against fluorescently labelled FITC-*Hi*SiaP (10 nM) identifies a shift in the signal for *Hi*SiaP from 3 S to ~7.5 S and ~10.5 S. This shift demonstrates binding to *Hi*SiaQM and identifies two bound species with different sedimentation coefficients. The two species are annotated with the most likely binding stoichiometries (one or two *Hi*SiaP monomers (red and grey) may be binding the dimeric species). **b**, Fitting a binding model to the data (Fraction bound = $[P]_{total}$ / $[P]_{total}$ + K_D) estimates a K_D of 65 µM (95% confidence interval = 62–69 µM, R^2 = 0.99).

Interestingly, the fluorescent signal shifted to two larger species. Based on the data for *Hi*SiaQM in L-MNG (**Figure 3a**), the two species at ~7.5 S and ~10.5 S likely correspond to monomeric *Hi*SiaQM with one *Hi*SiaP monomer bound and dimeric *Hi*SiaQM with either one or two *Hi*SiaP monomers bound (**Figure 6a**). To support this stoichiometry, we checked the in-solution oligomeric state of *Hi*SiaP, as there are examples of unusual TRAP substrate-binding proteins that form dimers (18,58). Both analytical ultracentrifugation (0.85 mg/mL, 25 µM) and small angle X-ray scattering experiments (injected at 12.3 mg/mL, 360 µM) suggest that *Hi*SiaP is monomeric in solution (**Supplementary Figure 10**).

To understand the observed complex formation, the interaction between *Hi*SiaP (PDB: 3B50) and *Hi*SiaQM (PDB: 8THI) was modelled using AlphaFold2 (59). The predicted binding mode does allow two *Hi*SiaP proteins to bind the parallel *Hi*SiaQM dimer without significant steric clashes

(**Supplementary Figure 11**) and each monomer has the same binding mode as the *Pp*SiaPQM model (33).

The resolution of our structure enabled us to model the side chains and rationalise previous mutagenic experiments designed to define the SiaP:SiaQM interaction. We demonstrated that the periplasmic-facing residue R292 in *Pp*SiaM is important for TRAP transporter activity and hypothesised that this residue is important for both the interaction with SiaP and rigidifying the scaffold-lateral arm helix junction (33). This residue is strictly conserved in sialic acid TRAP transporters but is not conserved across the TRAP transporter family (**Supplementary Figure 8**). Our structure shows that the equivalent residue in *Hi*SiaQM (R484) adopts a similar solvent-accessible conformation and participates in an ionic interaction with D480, which in turn is interacting with K236 (**Supplementary Figure 12**). Together these residues form a salt bridge network between two helices of the scaffold of the transporter. Consistent with this, mutation to R484E resulted in decreased bacterial growth, and reduced the binding of SiaP to SiaQM *in vitro* (27). Furthermore, mutations of residues on SiaP predicted to interact with this region reduce activity in both the *Hi*SiaPQM (27) and *Pp*SiaPQM (33) systems, highlighting the importance of this area for the transporter. It is clear that this region is important for SiaP recognition (also shown by the adjacent positioning of SiaP to this region in the complex model, **Supplementary Figure 11**) and may be further involved in modulating the conformational changes in SiaQM. Similarly, mutations R30E, S356Y and E429R all significantly reduced bacterial growth and SiaP binding (27). These mutations are consistent with disrupting the SiaP:SiaQM interaction as the residues are all solvent-accessible at the periplasmic surface of *Hi*SiaQM in our structure and are close to *Hi*SiaP in the complex model. All three residues are strictly conserved across the TRAP transporter family (**Supplementary Figure 8**) and our structure shows that R30 (SiaQ) and E429 (SiaM) form a salt bridge (~2.5 Å) between two helices of the scaffold to connect SiaQ and SiaM, highlighting their structural significance (**Supplementary Figure 12**). Overall, the *Hi*SiaPQM complex model is consistent with the mutagenesis of the *Hi*SiaPQM and *Pp*SiaPQM systems (27,33), but requires an experimental tripartite complex (SiaPQM) structure for validation.

Finally, the ability of related SiaPQM systems to substitute subunits was assessed using the transport assay (**Figure 5a, Figure 7a**). Two fused SiaPQM systems from the Pasteurellaceae family (*H. influenzae* and *Aggregatibacter actinomycetemcomitans*) were able to substitute the QM- and P-subunits and retain activity. With *Hi*SiaQM in the proteoliposome, there was no transport when *Pp*SiaP from the non-fused system was used (pink) but was fully functional when *Aa*SiaP was used (blue). We also substituted the QM-subunits: with *Aa*SiaQM in the proteoliposome, the transport was the same with *Hi*SiaP and *Aa*SiaP but slower in the *Aa*SiaPQM system than *Hi*SiaPQM,

suggesting that differences in the mechanisms (*e.g.*, the affinity of subunits or Na^+) may exist even in systems similar enough to exchange subunits. That there was no transport with *Hi*SiaQM and *Pp*SiaP follows previous work demonstrating that SiaP from *V. cholerae* did not function with *Hi*SiaQM (28). Structural analysis of the SiaP proteins from the fused and non-fused systems shows subtle differences in surface charge (**Figure 7b**), yet the activity results suggest the interacting surfaces have diverged enough to make them incompatible. It may also be that each system uses slightly different methods to engage the allosteric opening of SiaP.

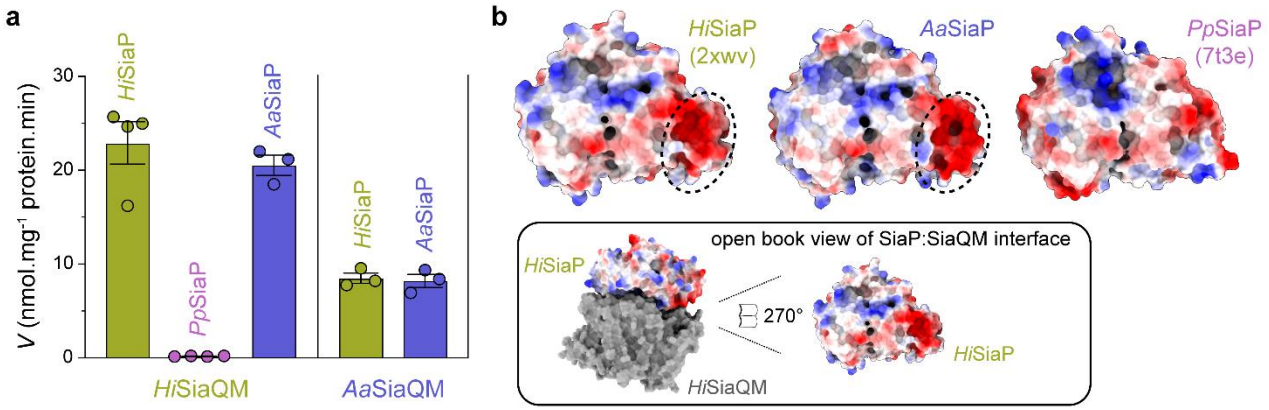

Figure 7 | Subunit substitution transport assays. **a**, Transport was measured with subunit substitution of *Hi*SiaPQM with the fused SiaPQM from *A. actinomycetemcomitans* (*Aa*) and the non-fused SiaPQM from *P. profundum* (*Pp*). Transport activity was measured in the presence of a membrane potential and a Na^+ gradient. The mean activity is shown as bars with SEM error from at least three technical replicates (n = 3 or 4). **b**, Electrostatic surface comparison of the putative SiaQM interaction surfaces of *Hi*SiaP, *Aa*SiaP and *Pp*SiaP. The SiaP proteins of the two fused systems have a greater area of negatively charged residues (red, circled) at the N-terminal lobe than in the non-fused system.

Discussion

Using the well-studied *Hi*SiaPQM TRAP as a model system (11,23,24,26-28), we: 1) determined a considerably higher resolution structure of the transmembrane subunits of this fused TRAP transporter, allowing us to now resolve side chains, lipids, the Na^+ ion binding sites, and the substrate binding site; 2) demonstrate that *Hi*SiaQM can form a dimeric configuration in maltoside detergents, amphipol and nanodiscs; and 3) determined the nature of the interaction between *Hi*SiaP and *Hi*SiaQM using biophysical methods. These experiments lead to many new conclusions that shape our understanding of how TRAP transporters function.

The 'elevator down' (inward-facing) conformation is preferred. The two previous SiaQM structures have relied on the presence of a megabody for structure determination, which made contacts with the periplasmic surface of the transport domain. This interaction may stabilise the protein in the observed

'elevator down' conformation. However, the dimeric structures we have presented have no other proteins bound, yet exist stably in the elevator down state, suggesting this is the most stable conformation.

Lipids associated with Hi*SiaQM are structurally and mechanistically important*. The structure of the fused *Hi*SiaQM confirms the presence of an extra transmembrane helix in the Q-subunit, compared to the non-fused TRAP systems that lack this helix. The extra transmembrane helix connects the small subunit to the large subunit via a short horizontal arm helix that runs parallel to the membrane. This horizontal helix is comprised of several positively charged residues that face the periplasm, contributing to an extra positive area on the surface of the transporter that is not seen in the non-fused *Pp*SiaQM. The horizontal helix may act similarly to the two arm helices and improve transport by increasing the steadiness of the scaffold of the transporter. The high-resolution structure of *Hi*SiaQM has identified well-defined lipids associated with tryptophan residues of the Q-subunits that form the dimer interface and a newly described single lipid in the binding pocket formed by the fusion helix. Both of these areas are likely important for anchoring the scaffold domain and allowing transport. As the single phospholipid is bound within the protein, it may also have a physiological role in P-subunit binding dynamics, as a mechanism of regulation depending on lipid type.

Hi*SiaQM can exist as a monomer or a dimer*. We demonstrate that *Hi*SiaQM can adopt both a monomeric and a dimeric configuration depending on the relative concentration of L-MNG detergent, with high concentrations favouring the monomer. This behaviour is characteristic of a self-association (**Supplementary Figure 1a**, **Figure 3a**). The formation of a stable dimeric species is also found in our amphipol structure, in other detergents, and in nanodiscs.

The parallel dimer is consistent with other elevator transporters, although the interface between the monomers is reduced. Notably, a related TAXI-TRAP transporter also appears to form a self-association (48) and the dicarboxylate transporter, VcINDY from *V. cholerae*, adopts a stable homodimeric configuration in crystal and in solution (38,39). VcINDY uses an elevator mechanism and cross-linking the dimer interface does not perturb transport, implying a lack of coupling between the monomers and an absence of large conformational changes at the interface (38). The dimerisation of VcINDY is used to stabilise the transport domains and allow the elevators to move up and down against the bound interface. Even with a small interface, a dimeric *Hi*SiaQM assembly may further stabilise the scaffold of the two monomeric units.

The antiparallel dimer is hard to rationalise from a physiological standpoint. Although not unprecedented *in vivo* with small bacterial multidrug transporters (60,61), an antiparallel structure makes little biological sense in the case of the TRAP transporter. In the antiparallel structure, the

inverted monomer displays the cytoplasmic face towards the periplasm and will not bind SiaP, which is required for transport. This structure could result from removing the protein from its native environment, where it is constrained by the cell membrane, and in the absence of the constraints of the membrane can rotate around the interface when solubilised by detergents.

The affinity of SiaP for SiaQM is weak. For the SiaPQM TRAP transporter, the role of SiaP is to capture Neu5Ac with high affinity and deliver it to SiaQM before leaving to bind more Neu5Ac. As a result, a high-affinity SiaPQM complex that has a slow SiaP off-rate is likely not desired. Neither is a low-affinity SiaPQM complex that has a slow SiaP on-rate, as SiaQM relies on binding SiaP for transport (**Figure 5a**). The K_D observed in our experiments may be representative of a system with a fast off-rate (and potentially a fast on-rate) for SiaP. The resulting K_D is not of high affinity, but the transport cycle is optimised as SiaP quickly binds SiaQM, delivers Neu5Ac, and then leaves without getting 'stuck' to the transporter. The fast off-rate would reflect the conformational coupling of SiaP to SiaQM as the open state of SiaP that occurs after delivering Neu5Ac has been shown to bind SiaQM less (27).

The determined K_D may also reflect the experimental conditions. If the transporter is often in the conformation we observe to be stabilised in the structures, then the residues on the periplasmic surface of SiaQM may not be accessible or correctly positioned for binding with the partner residues on SiaP. In addition to the effects of detergent, the experimental conditions do not provide a Na^+ gradient, which may have significant consequences on the positioning of SiaQM for interaction with SiaP. Under similar conditions, Peter et al. (27) estimated a comparable K_D of >1 μM, further indicating that the interaction affinity is low.

Conclusion

We have determined the oligomeric state of detergent solubilised *Hi*SiaQM and the structure of amphipol solubilised *Hi*SiaQM to near atomic resolution. In both membrane mimetics, we have observed a monomer-dimer self-association. The cryo-EM structure reveals the position of the extra transmembrane helix and shows that it is made of two sections with a positively charged periplasmic surface. This suggests that the extra helix may be involved in the interaction with SiaP, which has a predominantly negatively charged surface where it would likely bind the transporter. Furthermore, this work yields novel insights for drug design, as our structure can guide the design of inhibitors that block the SiaPQM interaction or use the system as a Trojan horse. In bacteria that rely solely on SiaPQM for obtaining Neu5Ac, such as *H. influenzae*, these inhibitors may have utility as antibacterial agents.

Materials and Methods

Cloning of the substrate-binding protein, SiaP, and the membrane bound protein, SiaQM.

The gene encoding SiaP from *H. influenzae* Rd KW20 was synthesised and cloned into the pET22b(+) vector to include a pelB leader sequence (Genscript). The pelB sequence signals the protein to the periplasm and is cleaved *in vivo* before purification. The gene encoding SiaQM from *H. influenzae* Rd KW20 was synthesised and cloned into the pBAD/HisA vector to include an N-terminal his-tag, Xpress epitope, enterokinase cleavage site and a linker sequence (GeneArt, Thermo Fisher Scientific). Full protein sequences for these genes are provided in **Supplementary Table 2**.

Expression and purification of the membrane embedded protein, SiaQM.

E. coli TOP10 cells containing the pBAD/HisA_*Hi*SiaQM plasmid were grown in Terrific Broth medium in 1.5 L cultures at 37 °C to OD_{600} = 1.4–1.8 before induction with 0.2% L-arabinose. Induced cultures were incubated for 3 h at 37 °C and 180 rpm. Cells were harvested by centrifugation at 8000 *g* for 10 min at 4 °C, snap frozen and stored at -80 °C. Cells were thawed at room temperature and added to resuspension buffer [1 x phosphate buffered saline (PBS) pH 7.4, 0.5 mg/mL lysozyme and 1 cOmplete protease inhibitor tablet (Roche) per 50 mL solution, or 1 mM phenylmethylsulfonyl fluoride (PMSF)]. Cells were resuspended and then lysed by sonication (70% amplitude, 0.5 s on / 0.5 s off). Unbroken cells and cell debris were removed by centrifugation at 18,000 *g* for 25 min at 4 °C twice. Membranes were harvested by ultracentrifugation at 210,000 *g* for 2 h at 4 °C, snap-frozen and stored at -80 °C.

Membranes were resuspended in membrane resuspension buffer (1 x PBS pH 7.4, 1 mM PMSF, 5 mM dithiothreitol and 6% v/v glycerol). Once resuspended, 2% w/v L-MNG or DDM was added for solubilisation for 2 h at 4 °C with gentle agitation. Insoluble material was removed by ultracentrifugation at 150,000 *g* for 1 h at 4 °C. The supernatant was collected, and imidazole was added to a final concentration of 20 mM. The sample was applied to a HisTrap FF 5 mL column (Cytiva) equilibrated with buffer A (70 mM Tris pH 8, 150 mM NaCl, 20 mM imidazole, 6% v/v glycerol, 5 mM β-mercaptoethanol (BME), 0.002–0.020% L-MNG (or 0.0348% DDM) and 0 or 5 mM Neu5Ac). The column was washed with 20 column volumes (CV) buffer A, then 10 CV 95% buffer A and 5% buffer B (70 mM Tris pH 8, 150 mM NaCl, 500 mM imidazole, 6% v/v glycerol, 5 mM BME, 0.002–0.020% L-MNG (or 0.0348% DDM) and 0 or 5 mM Neu5Ac) before eluting the protein with a gradient to 100% buffer B. Fractions identified by SDS-PAGE to contain *Hi*SiaQM were pooled and concentrated. Concentrated protein was applied to a HiLoad 16/600 Superdex 200 pg size exclusion column (Cytiva) equilibrated in buffer C [50 mM Tris pH 8, 150 mM NaCl, 0.002–

0.020% L-MNG (or 0.0348% DDM) and 0 or 5 mM Neu5Ac]. The final purified protein was obtained at a yield of 0.5 mg/L of *E. coli* culture and was at least 95% pure by SDS-PAGE (**Supplementary Figure 1b**).

Expression and purification of the substrate binding protein, SiaP.

E. coli BL21 (DE3) cells containing the pET22b(+) *Hi*SiaP plasmid were grown in M9 minimal medium with 0.1 mg/mL ampicillin in 1 L cultures at 26 °C to OD_{600} = 0.3 before induction with 1 mM IPTG. Induced cultures were incubated for 16 h at 26 °C and 180 rpm. Cells were harvested by centrifugation at 8,000 *g* for 10 min at 4 °C and resuspended in periplasmic extraction buffer [30 mM Tris pH 8, 20% w/v sucrose and 1 mM ethylenediaminetetraacetic acid (EDTA)] at room temperature (RT). The resuspension was incubated at RT for 10 min with shaking, then centrifuged at 13,000 *g* for 10 min at 4 °C. The supernatant was removed and the cell pellet rapidly resuspended in ice cold Milli-Q water. The resuspension was incubated for 10 min at 4 °C with shaking, then centrifuged as before. The supernatant was collected and PMSF was added to a concentration of 1 mM. The supernatant was filtered with a 0.2 µm filter and applied to a HiPrep Q FF 16/10 column (Cytiva) equilibrated in buffer D (50 mM Tris pH 8). The column was washed with 5 CV of buffer D before eluting the protein with a gradient to 100% buffer E (50 mM Tris pH 8, 1 M NaCl). SDS-PAGE was used to identify fractions containing *Hi*SiaP. These fractions were pooled, and ammonium sulphate was added to a concentration of 1 M. The protein was applied to a HiPrep Phenyl FF 16/10 column (Cytiva) equilibrated in buffer F (50 mM Tris pH 8, 1 M ammonium sulphate). The column was washed with 5 CV of buffer F before eluting the protein with a gradient to 100% buffer G (50 mM Tris pH 8, 150 mM NaCl). SDS-PAGE was used to identify fractions containing *Hi*SiaP. These fractions were pooled, concentrated, and applied to a HiLoad 16/600 Superdex 200 pg size exclusion column (Cytiva) equilibrated with buffer G. Fractions containing *Hi*SiaP were pooled and concentrated for use in experiments. SDS-PAGE was used to visually assess purity.

Reconstitution into nanodiscs.

The membrane scaffold protein cNW11 [purchased from Now Scientific (Boston, USA)] was used for the reconstitution of *Hi*SiaQM into nanodiscs. Lipid stocks of POPC (1-palmitoyl-2-oleoyl-glycero-3-phosphocholine) and POPG (1-palmitoyl-2-oleoyl-sn-glycero-3-phosphoglycerol) in chloroform were aliquoted in a 3:2 ratio and dried under nitrogen in a glass tube. The lipids were dissolved by heating and vortexing with buffer H (20 mM Tris pH 7.4, 100 mM NaCl, 0.5 mM EDTA and 160 mM sodium cholate). *Hi*SiaQM, cNW11 and lipids were incubated together at the three ratios for 1 h on ice with a final cholate concentration between 25–27 mM. For empty nanodiscs, a similar

reconstitution was set up with only cNW11 and lipids. Bio-Beads SM-2 were added (0.5 g to each 500 µL reconstitution) and the solution was incubated on ice for another 30 min before gentle rotation for 16 h at 4 °C. The solution was removed from the Bio-Beads with a 24-gauge needle and spun at 14,000 *g* to remove insoluble aggregates. The sample was concentrated and applied to a Superdex 200 Increase 10/300 GL column equilibrated with buffer I (20 mM Tris pH 7.4, 100 mM NaCl and 0.5 mM EDTA). Fractions of interest were concentrated and used for future experiments. SDS-PAGE was used to visually assess the presence of nanodisc reconstituted *Hi*SiaQM.

Reconstitution into amphipol.

Amphipol A8-35 (Anatrace) was added at 5 mg per 1 mg purified *Hi*SiaQM in L-MNG. Bio-Beads SM-2 were added at 100 mg per mL of the mixture before incubating overnight at 4 °C with gentle rotation. Following reconstitution, the amphipol bound protein was subjected to another size exclusion chromatography step, to remove unincorporated amphipol and any aggregated protein. Protein that eluted at a volume consistent with *Hi*SiaQM was pooled, concentrated, and used in experiments.

Western blotting.

A western blot was used to verify the bands containing *Hi*SiaQM on SDS-PAGE. *Hi*SiaQM was separated by SDS-PAGE and transferred to nitrocellulose using NuPAGE transfer buffer + 20% methanol. The transfer was performed for 15 min at 15 volts. Membranes were blocked with Tris buffered saline + 0.1% Tween 20 (TBST) and 2% bovine serum albumin (BSA) for 1 h at 4 °C. Mouse Xpress IgG monoclonal antibody (Invitrogen) was diluted to 1/2500 in TBST + 2% BSA and incubated with the membranes overnight at 4 °C. Membranes were washed with water before incubating with rabbit anti-mouse IgG secondary antibody (Sigma-Aldrich) with conjugated alkaline phosphatase at 1/15000 in TBST + 2% BSA for 1 h at RT. Membranes were washed with TBST for five min, three times. Detection was performed by incubating the membranes with NBT/BCIP substrate solution (Thermo Fisher Scientific) for 10 min. The reaction was stopped by rinsing the membranes in water.

Analytical ultracentrifugation.

Sedimentation velocity experiments were performed in a Beckman Coulter XL-I AUC instrument unless otherwise stated. Samples were loaded into 12 mm double sector cells with sapphire windows, then mounted in an An-60 Ti rotor. Sedimentation data were analysed with UltraScan 4.0 (62,63). Optimisation was performed by two-dimensional spectrum analysis (2DSA) (64,65) with

simultaneous removal of time- and radially invariant noise contributions and fitting of boundary conditions. Where appropriate, 2DSA solutions were subjected to parsimonious regularisation by genetic algorithm analysis (66).

For determining the oligomeric state of *Hi*SiaQM, the samples (0.40 mg/mL in L-MNG, 0.55 mg/mL in DDM) were in buffer G with either 20 times the critical micelle concentration (CMC) of L-MNG (0.02%, 200 µM) or 4 times the CMC of DDM (0.0348%, 0.68 mM). Buffer density and viscosity values were measured with a density meter and microviscometer (Anton Paar). Radial absorbance data were collected at 280 nm, 42,000 rpm and 20 °C (L-MNG) or 4 °C (DDM). Oligomeric state and bound detergent calculations were performed using a method similar to Henrickson et al. (67), utilising sedimentation and diffusion coefficients obtained from UltraScan (62,63).

For determining the *Hi*SiaQM species in the nanodisc and amphipol samples, the methods used were similar to that above. The nanodisc samples were in buffer I. The data were collected at 280 nm, 46,000 rpm and 10 °C. The amphipol sample was in buffer G. The data were collected at 0.27 mg/mL, 280 nm (intensity data), 40,000 rpm and 20 °C in a Beckman Coulter Optima AUC instrument at the Canadian Center for Hydrodynamics at the University of Lethbridge.

For determining the oligomeric state of *Hi*SiaP, the samples were in buffer G and buffer G + 5 mM Neu5Ac. Buffer density and viscosity values were estimated with UltraScan (62) or measured with a density meter and microviscometer (Anton Paar). The data were collected at 280 nm, 42,000 or 50,000 rpm and 20 °C.

Fluorescence detection analytical ultracentrifugation.

Experiments were performed with FITC labelled *Hi*SiaP and a concentration series of *Hi*SiaQM. The FITC labelling was optimised to produce a ratio of 0.93 (~1) moles of FITC per mole of protein. A Beckman Coulter XL-A AUC instrument with a fluorescence detection system (AVIV Biomedical) was used with an An-50 Ti rotor at the University of Melbourne, Australia. To generate an artificial bottom, 50 µL of FC43 fluorinert oil was loaded into the bottom of each cell. The samples (350 µL) in buffer G + 0.002% L-MNG and 5 mM Neu5Ac were loaded into 12 mm double sector cells. *Hi*SiaP was kept constant at 10 nM and *Hi*SiaQM was varied across 14 concentrations (2-fold dilutions from 40 µM to 4.9 nM). The samples were incubated for an hour at room temperature, then run at 50,000 rpm and 20 °C in fluorescence mode.

Proteoliposome assays.

Purified *Hi*SiaQM was reconstituted using a batch-wise detergent removal procedure as previously described (54,68). In brief, 50 μg of *Hi*SiaQM was mixed with 120 μL of 10% $C_{12}E_8$ and 100 μL of 10% egg yolk phospholipids (w/v) in the form of sonicated liposomes as previously described (69), 50 mM of K^+-gluconate and 20 mM HEPES/Tris pH 7.0 in a final volume of 700 μL. The reconstitution mixture was incubated with 0.5 g Amberlite XAD-4 resin under rotatory stirring (1,200 rev/min) at 25 °C for 40 min (69).

After reconstitution, 600 μL of proteoliposomes were loaded onto a Sephadex G-75 column (0.7 cm diameter × 15 cm height) pre-equilibrated with 20 mM HEPES/Tris pH 7.0 with 100 mM sucrose to balance the internal osmolarity. Then, valinomycin (0.75 μg/mg phospholipid) prepared in ethanol was added to the eluted proteoliposomes to generate a K^+ diffusion potential, as previously described (54). For a standard measurement, after 10 s of incubation with valinomycin transport was started by adding 5 μM [^{3}H]-Neu5Ac to 100 μL proteoliposomes in the presence of 50 mM Na^+-gluconate and 0.5 μM of *Hi*SiaP. Experiments were also performed varying the [Na^+-gluconate] and SiaP species to determine their effect on transport. The transport assay was terminated by loading each proteoliposome sample (100 μL) on a Sephadex G-75 column (0.6 cm diameter × 8 cm height) to remove the external radioactivity. Proteoliposomes were eluted with 1 mL 50 mM NaCl and collected in 4 mL of scintillation mixture, vortexed and counted. The radioactivity taken up in controls performed with empty liposomes, *i.e.*, liposomes without incorporated protein, was negligible with respect to the data obtained with proteoliposomes, *i.e.*, liposomes with incorporated proteins. All measurements are presented as means ± SEM from independent experiments as specified in the figure legends. Data analysis and graphs of data and fit were produced using GraphPad Prism (version 9).

Single particle cryogenic electron microscopy data collection, processing and map refinement.

*Hi*SiaQM was purified as before but with buffers containing a low concentration of L-MNG detergent (0.002%, 20 μM) to produce a population favouring dimeric particles (see **Figure 2, blue trace**). The protein was exchanged into amphipol A8-35, concentrated, and frozen at -80 °C until use. The protein was thawed, centrifuged to remove any aggregates, concentrated to 4.1 mg/mL, applied to a glow-discharged (Gatan Solarus) Cu 2/1 carbon Quantifoil grid (Electron-microscopy Sciences), and blotted using a Vitrobot Mark IV (Thermo Fisher Scientific) for 3.5 s, at 4 °C, and with 100% humidity before vitrification in liquid ethane. The grid was screened for ice quality and particle distribution on a Talos Arctica microscope. A 14,281-image dataset was collected. The data collection parameters are provided in **Supplementary Table 1**.

All cryo-EM data processing was performed using CryoSPARC v.3.2.0 (70) (**Supplementary Figure**

2). In brief, movie frames were aligned using patch motion correction with a B-factor of 500, and then contrast transfer function (CTF) estimations were made using the patch CTF estimation tool. Initially, 84,871 particles were picked from 295 micrographs using the Blob Picker tool and extracted. These particles were 2D classified into 50 classes, and 10 of these 2D classes were selected and used as a template for automated particle picking using the Template Picker tool, where 3,957,461 particles were picked from 14,281 micrographs. Particles were inspected with the Inspect Picks tool using an NCC Score Threshold of 0.1, and a Local Power range of 29,159 to 62,161. A total of 2,950,415 particles were extracted with a box size of 400 pixels and Fourier cropped to 200 pixels. The extracted particles were then sorted using iterative rounds of 2D classification, where the best 39 classes showing some structural details were selected, retaining 618,442 particles. The particles were subjected to *ab initio* reconstruction separated into four classes. The two best 3D reconstructions represent dimers that oligomerised in two different ways—an antiparallel dimer and a parallel dimer, for which we had 225,044 and 220,810 particles, respectively. At this point, the datasets were separated for further processing. For each set of data, the reconstructions were used as a reference model for iterative rounds of non-uniform refinement, allowing a 2.99 Å map to be reconstructed for the antiparallel dimer and a 3.36 Å map to be reconstructed for the parallel dimer. For refinement of the antiparallel dimer, C2 symmetry was imposed. The final rounds of refinement were conducted using unbinned particles. The model was built using an initial model from AlphaFold (59), which was fit to the maps using Namdinator (71), ISOLDE (72) and Coot (73) were both used for further model building. A summary of the statistics for data processing, refinement, and validation is shown in **Supplementary Table 1**.

Small-angle X-ray scattering.

Small angle X-ray scattering data were collected on the SAXS/WAXS beamline equipped with a Pilatus 1 M detector (170 mm × 170 mm, effective pixel size, 172 μm × 172 μm) at the Australian Synchrotron. A sample detector distance of 1600 mm was used, providing a q range of 0.05–0.5 $Å^{-1}$. *Hi*SiaP (50 μL at 12.3 mg/mL) was measured in buffer G + 0.1% w/v NaN_3 and buffer I + 0.1% w/v NaN_3 and 5 mM Neu5Ac. Each sample was injected onto a Superdex 200 Increase 5/150 GL column (Cytiva) before data collection with 1 s exposures. Buffer subtraction and data analysis were performed in CHROMIXS and PRIMUS from the ATSAS program suite (74).

Software.

Molecular graphics and analyses were made with Pymol (75) and UCSF ChimeraX (76). Figures were made with Adobe Illustrator.

Acknowledgements

This research was undertaken in part using the MX2 beamlines, and made use of the Australian Cancer Research Foundation (ACRF) detector, as well as the SAXS beamline at the Australian Synchrotron, part of ANSTO. R.A.N. and M.J.C. acknowledge the Canterbury Medical Research Foundation (CMRF) for Major Project Grant funding and the Biomolecular Interaction Centre (UC) for funding support. This research was supported by an AINSE Ltd. Postgraduate Research Award (PGRA) to M.J.C. and J.S.D. R.C.J.D. acknowledges the following for funding support, in part: 1) the Marsden Fund, managed by Royal Society Te Apārangi (contract UOC1506); 2) a Ministry of Business, Innovation and Employment Smart Ideas grant (contract UOCX1706); and 3) the Biomolecular Interaction Centre (UC). We thank Yee-Foong Mok and Amy Henrickson for their assistance with AUC experiments. Cryo-EM data were collected at the Cryo-EM Swedish National Facility funded by the Knut and Alice Wallenberg Foundation, the Family Erling Persson and Kempe Foundations, SciLifeLab, Stockholm University and Umeå University.

Competing interests

R.F. is currently employed by AstraZeneca.

References

1. Ren, Q., and Paulsen, I. T. (2005) Comparative analyses of fundamental differences in membrane transport capabilities in prokaryotes and eukaryotes. *PLoS Comput Biol* **1**, e27
2. Pao, S. S., Paulsen, I. T., and Saier Jr, M. H. (1998) Major facilitator superfamily. *Microbiology and molecular biology reviews* **62**, 1-34
3. Reizer, J., Reizer, A., and Saier Jr, M. H. (1994) A functional superfamily of sodium/solute symporters. *Biochimica et Biophysica Acta (BBA)-Reviews on Biomembranes* **1197**, 133-166
4. Drew, D., North, R. A., Nagarathinam, K., and Tanabe, M. (2021) Structures and General Transport Mechanisms by the Major Facilitator Superfamily (MFS). *Chemical reviews* **121**, 5289-5335
5. Bosshart, P. D., and Fotiadis, D. (2019) Secondary active transporters. *Bacterial Cell Walls and Membranes*, 275-299
6. Henriquez, T., Wirtz, L., Su, D., and Jung, H. (2021) Prokaryotic Solute/Sodium Symporters: Versatile Functions and Mechanisms of a Transporter Family. *International Journal of Molecular Sciences* **22**, 1880
7. Vimr, E. R. (2013) Unified theory of bacterial sialometabolism: how and why bacteria metabolize host sialic acids. *International Scholarly Research Notices* **2013**
8. Apicella, M. A. (2012) Nontypeable Haemophilus influenzae: the role of N-acetyl-5-neuraminic acid in biology. *Front Cell Infect Microbiol* **2**, 19
9. Cohen, M., and Varki, A. (2010) The sialome—far more than the sum of its parts. *Omics: a journal of integrative biology* **14**, 455-464
10. McDonald, N. D., Lubin, J.-B., Chowdhury, N., and Boyd, E. F. (2016) Host-derived sialic acids are an important nutrient source required for optimal bacterial fitness in vivo. *MBio* **7**, e02237-02215
11. Severi, E., Randle, G., Kivlin, P., Whitfield, K., Young, R., Moxon, R., Kelly, D., Hood, D., and Thomas, G. H. (2005) Sialic acid transport in Haemophilus influenzae is essential for lipopolysaccharide sialylation and serum resistance and is dependent on a novel tripartite ATP-independent periplasmic transporter. *Mol Microbiol* **58**, 1173-1185
12. Allen, S., Zaleski, A., Johnston, J. W., Gibson, B. W., and Apicella, M. A. (2005) Novel sialic acid transporter of Haemophilus influenzae. *Infection and immunity* **73**, 5291-5300
13. Vimr, E., Lichtensteiger, C., and Steenbergen, S. (2000) Sialic acid metabolism's dual function in Haemophilus influenzae. *Mol Microbiol* **36**, 1113-1123
14. Jenkins, G. A., Figueira, M., Kumar, G. A., Sweetman, W. A., Makepeace, K., Pelton, S. I., Moxon, R., and Hood, D. W. (2010) Sialic acid mediated transcriptional modulation of a highly conserved sialometabolism gene cluster in Haemophilus influenzae and its effect on virulence. *BMC Microbiol* **10**, 48
15. Bozzola, T., Scalise, M., Larsson, C. U., Newton-Vesty, M. C., Rovegno, C., Mitra, A., Cramer, J., Wahlgren, W. Y., Radhakrishnan Santhakumari, P., Johnsson, R. E., Schwardt, O., Ernst, B., Friemann, R., Dobson, R. C. J., Indiveri, C., Schelin, J., Nilsson, U. J., and Ellervik, U. (2022) Sialic Acid Derivatives Inhibit SiaT Transporters and Delay Bacterial Growth. *ACS Chem Biol* **17**, 1890-1900
16. Kelly, D. J., and Thomas, G. H. (2001) The tripartite ATP-independent periplasmic (TRAP) transporters of bacteria and archaea. *FEMS microbiology reviews* **25**, 405-424
17. Rosa, L. T., Bianconi, M. E., Thomas, G. H., and Kelly, D. J. (2018) Tripartite ATP-independent periplasmic (TRAP) transporters and tripartite tricarboxylate transporters (TTT): from uptake to pathogenicity. *Frontiers in cellular and infection microbiology* **8**, 33
18. Vetting, M. W., Al-Obaidi, N., Zhao, S., San Francisco, B., Kim, J., Wichelecki, D. J., Bouvier, J. T., Solbiati, J. O., Vu, H., and Zhang, X. (2015) Experimental strategies for functional annotation and metabolism discovery: targeted screening of solute binding proteins and unbiased panning of metabolomes. *Biochemistry* **54**, 909-931

19. Mulligan, C., Fischer, M., and Thomas, G. H. (2011) Tripartite ATP-independent periplasmic (TRAP) transporters in bacteria and archaea. *FEMS microbiology reviews* **35**, 68-86
20. Mulligan, C., Leech, A. P., Kelly, D. J., and Thomas, G. H. (2012) The membrane proteins SiaQ and SiaM form an essential stoichiometric complex in the sialic acid tripartite ATP-independent periplasmic (TRAP) transporter SiaPQM (VC1777–1779) from Vibrio cholerae. *Journal of Biological Chemistry* **287**, 3598-3608
21. Blum, M., Chang, H. Y., Chuguransky, S., Grego, T., Kandasaamy, S., Mitchell, A., Nuka, G., Paysan-Lafosse, T., Qureshi, M., Raj, S., Richardson, L., Salazar, G. A., Williams, L., Bork, P., Bridge, A., Gough, J., Haft, D. H., Letunic, I., Marchler-Bauer, A., Mi, H., Natale, D. A., Necci, M., Orengo, C. A., Pandurangan, A. P., Rivoire, C., Sigrist, C. J. A., Sillitoe, I., Thanki, N., Thomas, P. D., Tosatto, S. C. E., Wu, C. H., Bateman, A., and Finn, R. D. (2021) The InterPro protein families and domains database: 20 years on. *Nucleic Acids Res* **49**, D344-d354
22. Scheepers, G. H., Lycklama a Nijeholt, J. A., and Poolman, B. (2016) An updated structural classification of substrate-binding proteins. *FEBS letters* **590**, 4393-4401
23. Muller, A., Severi, E., Mulligan, C., Watts, A. G., Kelly, D. J., Wilson, K. S., Wilkinson, A. J., and Thomas, G. H. (2006) Conservation of structure and mechanism in primary and secondary transporters exemplified by SiaP, a sialic acid binding virulence factor from Haemophilus influenzae. *Journal of Biological Chemistry* **281**, 22212-22222
24. Johnston, J. W., Coussens, N. P., Allen, S., Houtman, J. C., Turner, K. H., Zaleski, A., Ramaswamy, S., Gibson, B. W., and Apicella, M. A. (2008) Characterization of the N-acetyl-5-neuraminic acid-binding site of the extracytoplasmic solute receptor (SiaP) of nontypeable Haemophilus influenzae strain 2019. *Journal of Biological Chemistry* **283**, 855-865
25. Gangi Setty, T., Cho, C., Govindappa, S., Apicella, M. A., and Ramaswamy, S. (2014) Bacterial periplasmic sialic acid-binding proteins exhibit a conserved binding site. *Acta Crystallographica Section D: Biological Crystallography* **70**, 1801-1811
26. Fischer, M., Hopkins, A. P., Severi, E., Hawkhead, J., Bawdon, D., Watts, A. G., Hubbard, R. E., and Thomas, G. H. (2015) Tripartite ATP-independent Periplasmic (TRAP) Transporters Use an Arginine-mediated Selectivity Filter for High Affinity Substrate Binding. *J Biol Chem* **290**, 27113-27123
27. Peter, M. F., Ruland, J. A., Depping, P., Schneberger, N., Severi, E., Moecking, J., Gatterdam, K., Tindall, S., Durand, A., Heinz, V., Siebrasse, J. P., Koenig, P.-A., Geyer, M., Ziegler, C., Kubitscheck, U., Thomas, G. H., and Hagelueken, G. (2022) Structural and mechanistic analysis of a tripartite ATP-independent periplasmic TRAP transporter. *Nature Communications* **13**, 4471
28. Mulligan, C., Geertsma, E. R., Severi, E., Kelly, D. J., Poolman, B., and Thomas, G. H. (2009) The substrate-binding protein imposes directionality on an electrochemical sodium gradient-driven TRAP transporter. *Proceedings of the National Academy of Sciences* **106**, 1778-1783
29. Lichtensteiger, C. A., and Vimr, E. R. (1997) Neuraminidase (sialidase) activity of Haemophilus parasuis. *FEMS Microbiology Letters* **152**, 269-274
30. Vachon, V., Lyew, D. J., and Coulton, J. W. (1985) Transmembrane permeability channels across the outer membrane of Haemophilus influenzae type b. *Journal of bacteriology* **162**, 918-924
31. Munson Jr, R., Brodeur, B., Chong, P., Grass, S., Martin, D., and Proulx, C. (1992) Outer Membrane Proteins PI and P2 of Haemophilus influenzae Type b: Structure and Identification of Surface-Exposed Epitopes. *Journal of Infectious Diseases* **165**, S86-S89
32. Wirth, C., Condemine, G., Boiteux, C., Bernèche, S., Schirmer, T., and Peneff, C. M. (2009) NanC crystal structure, a model for outer-membrane channels of the acidic sugar-specific KdgM porin family. *Journal of molecular biology* **394**, 718-731

33. Davies, J. S., Currie, M. J., North, R. A., Scalise, M., Wright, J. D., Copping, J. M., Remus, D. M., Gulati, A., Morado, D. R., Jamieson, S. A., Newton-Vesty, M. C., Abeysekera, G. S., Ramaswamy, S., Friemann, R., Wakatsuki, S., Allison, J. R., Indiveri, C., Drew, D., Mace, P. D., and Dobson, R. C. J. (2023) Structure and mechanism of a tripartite ATP-independent periplasmic TRAP transporter. *Nature Communications* **14**, 1120
34. Punjani, A., and Fleet, D. J. (2021) 3D variability analysis: Resolving continuous flexibility and discrete heterogeneity from single particle cryo-EM. *Journal of Structural Biology* **213**, 107702
35. Krissinel, E., and Henrick, K. (2007) Inference of Macromolecular Assemblies from Crystalline State. *Journal of Molecular Biology* **372**, 774-797
36. Gupta, K., Donlan, J. A. C., Hopper, J. T. S., Uzdavinys, P., Landreh, M., Struwe, W. B., Drew, D., Baldwin, A. J., Stansfeld, P. J., and Robinson, C. V. (2017) The role of interfacial lipids in stabilizing membrane protein oligomers. *Nature* **541**, 421-424
37. Chang, Y.-N., Jaumann, E. A., Reichel, K., Hartmann, J., Oliver, D., Hummer, G., Joseph, B., and Geertsma, E. R. (2019) Structural basis for functional interactions in dimers of SLC26 transporters. *Nature Communications* **10**, 2032
38. Mulligan, C., Fenollar-Ferrer, C., Fitzgerald, G. A., Vergara-Jaque, A., Kaufmann, D., Li, Y., Forrest, L. R., and Mindell, J. A. (2016) The bacterial dicarboxylate transporter VcINDY uses a two-domain elevator-type mechanism. *Nature structural & molecular biology* **23**, 256-263
39. Mancusso, R., Gregorio, G. G., Liu, Q., and Wang, D.-N. (2012) Structure and mechanism of a bacterial sodium-dependent dicarboxylate transporter. *Nature* **491**, 622-626
40. Nie, R., Stark, S., Symersky, J., Kaplan, R. S., and Lu, M. (2017) Structure and function of the divalent anion/Na+ symporter from Vibrio cholerae and a humanized variant. *Nature communications* **8**, 1-10
41. Su, C.-C., Bolla, J. R., Kumar, N., Radhakrishnan, A., Long, F., Delmar, J. A., Chou, T.-H., Rajashankar, K. R., Shafer, W. M., and Edward, W. Y. (2015) Structure and function of Neisseria gonorrhoeae MtrF illuminates a class of antimetabolite efflux pumps. *Cell reports* **11**, 61-70
42. Bolla, J. R., Su, C.-C., Delmar, J. A., Radhakrishnan, A., Kumar, N., Chou, T.-H., Long, F., Rajashankar, K. R., and Edward, W. Y. (2015) Crystal structure of the Alcanivorax borkumensis YdaH transporter reveals an unusual topology. *Nature communications* **6**, 1-10
43. Kaback, H. R. (2005) Structure and mechanism of the lactose permease. *Comptes rendus biologies* **328**, 557-567
44. Faham, S., Watanabe, A., Besserer, G. M., Cascio, D., Specht, A., Hirayama, B. A., Wright, E. M., and Abramson, J. (2008) The crystal structure of a sodium galactose transporter reveals mechanistic insights into Na+/sugar symport. *Science* **321**, 810-814
45. Perez, C., Khafizov, K., Forrest, L. R., Krämer, R., and Ziegler, C. (2011) The role of trimerization in the osmoregulated betaine transporter BetP. *EMBO reports* **12**, 804-810
46. Yernool, D., Boudker, O., Jin, Y., and Gouaux, E. (2004) Structure of a glutamate transporter homologue from Pyrococcus horikoshii. *Nature* **431**, 811-818
47. Vergara-Jaque, A., Fenollar-Ferrer, C., Mulligan, C., Mindell, J. A., and Forrest, L. R. (2015) Family resemblances: A common fold for some dimeric ion-coupled secondary transporters. *J Gen Physiol* **146**, 423-434
48. Roden, A., Engelin, M. K., Pos, K. M., and Geertsma, E. R. (2023) Membrane-anchored substrate binding proteins are deployed in secondary TAXI transporters. *Biological Chemistry*
49. Nasr, M. L., Baptista, D., Strauss, M., Sun, Z.-Y. J., Grigoriu, S., Huser, S., Plückthun, A., Hagn, F., Walz, T., and Hogle, J. M. (2017) Covalently circularized nanodiscs for studying membrane proteins and viral entry. *Nature methods* **14**, 49-52
50. Nji, E., Chatzikyriakidou, Y., Landreh, M., and Drew, D. (2018) An engineered thermal-shift screen reveals specific lipid preferences of eukaryotic and prokaryotic membrane

proteins. *Nature Communications* **9**, 4253
51. Landreh, M., Marklund, E. G., Uzdavinys, P., Degiacomi, M. T., Coincon, M., Gault, J., Gupta, K., Liko, I., Benesch, J. L. P., Drew, D., and Robinson, C. V. (2017) Integrating mass spectrometry with MD simulations reveals the role of lipids in Na+/H+ antiporters. *Nature Communications* **8**, 13993
52. Matsuoka, R., Fudim, R., Jung, S., Zhang, C., Bazzone, A., Chatzikyriakidou, Y., Robinson, C. V., Nomura, N., Iwata, S., Landreh, M., Orellana, L., Beckstein, O., and Drew, D. (2022) Structure, mechanism and lipid-mediated remodeling of the mammalian Na+/H+ exchanger NHA2. *Nature Structural & Molecular Biology* **29**, 108-120
53. de Jesus, A. J., and Allen, T. W. (2013) The role of tryptophan side chains in membrane protein anchoring and hydrophobic mismatch. *Biochimica et Biophysica Acta (BBA) - Biomembranes* **1828**, 864-876
54. Wahlgren, W. Y., Dunevall, E., North, R. A., Paz, A., Scalise, M., Bisignano, P., Bengtsson-Palme, J., Goyal, P., Claesson, E., and Caing-Carlsson, R. (2018) Substrate-bound outward-open structure of a Na+-coupled sialic acid symporter reveals a new Na+ site. *Nature communications* **9**, 1-14
55. Huysmans, G. H. M., Ciftci, D., Wang, X., Blanchard, S. C., and Boudker, O. (2021) The high-energy transition state of the glutamate transporter homologue GltPh. *The EMBO Journal* **40**, e105415
56. Zheng, H., Chordia, M. D., Cooper, D. R., Chruszcz, M., Müller, P., Sheldrick, G. M., and Minor, W. (2014) Validation of metal-binding sites in macromolecular structures with the CheckMyMetal web server. *Nat Protoc* **9**, 156-170
57. Brown, I. D. (2009) Recent developments in the methods and applications of the bond valence model. *Chem Rev* **109**, 6858-6919
58. Gonin, S., Arnoux, P., Pierru, B., Lavergne, J., Alonso, B., Sabaty, M., and Pignol, D. (2007) Crystal structures of an Extracytoplasmic Solute Receptor from a TRAP transporter in its open and closed forms reveal a helix-swapped dimer requiring a cation for alpha-keto acid binding. *BMC Struct Biol* **7**, 11
59. Jumper, J., Evans, R., Pritzel, A., Green, T., Figurnov, M., Ronneberger, O., Tunyasuvunakool, K., Bates, R., Žídek, A., Potapenko, A., Bridgland, A., Meyer, C., Kohl, S. A. A., Ballard, A. J., Cowie, A., Romera-Paredes, B., Nikolov, S., Jain, R., Adler, J., Back, T., Petersen, S., Reiman, D., Clancy, E., Zielinski, M., Steinegger, M., Pacholska, M., Berghammer, T., Bodenstein, S., Silver, D., Vinyals, O., Senior, A. W., Kavukcuoglu, K., Kohli, P., and Hassabis, D. (2021) Highly accurate protein structure prediction with AlphaFold. *Nature* **596**, 583-589
60. Lloris-Garcerá, P., Bianchi, F., Slusky, J. S., Seppälä, S., Daley, D. O., and von Heijne, G. (2012) Antiparallel dimers of the small multidrug resistance protein EmrE are more stable than parallel dimers. *J Biol Chem* **287**, 26052-26059
61. Fluman, N., Tobiasson, V., and von Heijne, G. (2017) Stable membrane orientations of small dual-topology membrane proteins. *Proc Natl Acad Sci U S A* **114**, 7987-7992
62. Demeler, B., and Gorbet, G. E. (2016) Analytical Ultracentrifugation Data Analysis with UltraScan-III. in *Analytical Ultracentrifugation: Instrumentation, Software, and Applications* (Uchiyama, S., Arisaka, F., Stafford, W. F., and Laue, T. eds.), Springer Japan, Tokyo. pp 119-143
63. Dubbs, B., Zollars, D., Gorbet, G. E., Brookes, E. H., Savelyev, A., Mortezazadeh, S., and Demeler, B. UltraScan-III - a framework for hydrodynamic modeling. https://github.com/ehb54/ultrascan3.
64. Brookes, E. H., Boppana, R. V., and Demeler, B. (2006) Computing large sparse multivariate optimization problems with an application in biophysics. in *Proceedings of the 2006 ACM/IEEE conference on Supercomputing*, Association for Computing Machinery, Tampa, Florida
65. Brookes, E., Cao, W., and Demeler, B. (2010) A two-dimensional spectrum analysis for

sedimentation velocity experiments of mixtures with heterogeneity in molecular weight and shape. *Eur Biophys J* **39**, 405-414

66. Brookes, E. H., and Demeler, B. (2007) Parsimonious regularization using genetic algorithms applied to the analysis of analytical ultracentrifugation experiments. in *Proceedings of the 9th annual conference on Genetic and evolutionary computation*, Association for Computing Machinery, London, England

67. Henrickson, A., Montina, T., Hazendonk, P., Lomonte, B., Neves-Ferreira, A. G. C., and Demeler, B. (2023) SDS-induced hexameric oligomerization of myotoxin-II from Bothrops asper assessed by sedimentation velocity and nuclear magnetic resonance. *European Biophysics Journal*

68. North, R. A., Wahlgren, W. Y., Remus, D. M., Scalise, M., Kessans, S. A., Dunevall, E., Claesson, E., Soares da Costa, T. P., Perugini, M. A., and Ramaswamy, S. (2018) The sodium sialic acid symporter from Staphylococcus aureus has altered substrate specificity. *Frontiers in chemistry* **6**, 233

69. Scalise, M., Galluccio, M., Pochini, L., Console, L., Barile, M., Giangregorio, N., Tonazzi, A., and Indiveri, C. (2017) Studying interactions of drugs with cell membrane nutrient transporters: new frontiers of proteoliposome nanotechnology. *Current pharmaceutical design* **23**, 3871-3883

70. Punjani, A., Rubinstein, J. L., Fleet, D. J., and Brubaker, M. A. (2017) cryoSPARC: algorithms for rapid unsupervised cryo-EM structure determination. *Nature methods* **14**, 290-296

71. Kidmose, R. T., Juhl, J., Nissen, P., Boesen, T., Karlsen, J. L., and Pedersen, B. P. (2019) Namdinator–automatic molecular dynamics flexible fitting of structural models into cryo-EM and crystallography experimental maps. *IUCrJ* **6**, 526-531

72. Croll, T. I. (2018) ISOLDE: a physically realistic environment for model building into low-resolution electron-density maps. *Acta Crystallogr D Struct Biol* **74**, 519-530

73. Emsley, P., Lohkamp, B., Scott, W. G., and Cowtan, K. (2010) Features and development of Coot. *Acta Crystallogr D Biol Crystallogr* **66**, 486-501

74. Manalastas-Cantos, K., Konarev, P. V., Hajizadeh, N. R., Kikhney, A. G., Petoukhov, M. V., Molodenskiy, D. S., Panjkovich, A., Mertens, H. D., Gruzinov, A., and Borges, C. (2021) ATSAS 3.0: expanded functionality and new tools for small-angle scattering data analysis. *Journal of Applied Crystallography* **54**

75. The PyMOL Molecular Graphics System, Version 2.1.1 Schrödinger, LLC.

76. Pettersen, E. F., Goddard, T. D., Huang, C. C., Meng, E. C., Couch, G. S., Croll, T. I., Morris, J. H., and Ferrin, T. E. (2021) UCSF ChimeraX: Structure visualization for researchers, educators, and developers. *Protein Sci* **30**, 70-82

77. Brautigam, C. A. (2015) Calculations and publication-quality illustrations for analytical ultracentrifugation data. *Methods in enzymology* **562**, 109-133

78. Ebel, C. (2011) Sedimentation velocity to characterize surfactants and solubilized membrane proteins. *Methods* **54**, 56-66

79. Le Maire, M., Arnou, B., Olesen, C., Georgin, D., Ebel, C., and Møller, J. V. (2008) Gel chromatography and analytical ultracentrifugation to determine the extent of detergent binding and aggregation, and Stokes radius of membrane proteins using sarcoplasmic reticulum Ca 2+–ATPase as an example. *Nature protocols* **3**, 1782-1795

80. Le Roy, A., Wang, K., Schaack, B., Schuck, P., Breyton, C., and Ebel, C. (2015) AUC and small-angle scattering for membrane proteins. *Methods in enzymology* **562**, 257-286

81. Salvay, A. G., Santamaria, M., Le Maire, M., and Ebel, C. (2007) Analytical ultracentrifugation sedimentation velocity for the characterization of detergent-solubilized membrane proteins Ca++-ATPase and ExbB. *Journal of biological physics* **33**, 399-419

82. Lassmann, T. (2019) Kalign 3: multiple sequence alignment of large data sets. *Bioinformatics* **36**, 1928-1929

83. Waterhouse, A. M., Procter, J. B., Martin, D. M. A., Clamp, M., and Barton, G. J. (2009)

Jalview Version 2—a multiple sequence alignment editor and analysis workbench. *Bioinformatics* **25**, 1189-1191

84. Terwilliger, T. C., Sobolev, O. V., Afonine, P. V., and Adams, P. D. (2018) Automated map sharpening by maximization of detail and connectivity. *Acta Crystallogr D Struct Biol* **74**, 545-559